

THE IMPACT OF VECTOR RESONANT RELAXATION ON THE EVOLUTION OF BINARIES NEAR A MASSIVE BLACK HOLE: IMPLICATIONS FOR GRAVITATIONAL WAVE SOURCES

ADRIAN S. HAMERS¹, BEN BAR-OR¹, CRISTOBAL PETROVICH^{2,3}, FABIO ANTONINI⁴

¹Institute for Advanced Study, School of Natural Sciences, Einstein Drive, Princeton, NJ 08540, USA

²Canadian Institute for Theoretical Astrophysics, University of Toronto, 60 St George Street, ON M5S 3H8, Canada

³Centre for Planetary Sciences, Department of Physical & Environmental Sciences, University of Toronto at Scarborough, Toronto, Ontario M1C 1A4, Canada

⁴Astrophysics Research Group, Faculty of Engineering and Physical Sciences, University of Surrey, Guildford, Surrey, GU2 7XH, United Kingdom

Draft version August 15, 2018

Abstract

Binaries within the sphere of influence of a massive black hole (MBH) in galactic nuclei are susceptible to the Lidov-Kozai (LK) mechanism, which can drive orbits to high eccentricities and trigger strong interactions within the binary such as the emission of gravitational waves (GWs), and mergers of compact objects. These events are potential sources for GW detectors such as Advanced LIGO and VIRGO. The LK mechanism is only effective if the binary is highly inclined with respect to its orbit around the MBH (within a few degrees of 90°), implying low rates. However, close to an MBH, torques from the stellar cluster give rise to the process of vector resonant relaxation (VRR). VRR can bring a low-inclination binary into an ‘active’ LK regime in which high eccentricities and strong interactions are triggered in the binary. Here, we study the coupled LK-VRR dynamics, with implications for LIGO and VIRGO GW sources. We carry out Monte Carlo simulations and find that the merger fraction enhancement due to LK-VRR dynamics is up to a factor of ~ 10 for the lower end of assumed MBH masses ($M_{\bullet} = 10^4 M_{\odot}$), and decreases sharply with increasing M_{\bullet} . We find that, even in our most optimistic scenario, the baseline BH-BH merger rate is small, and the enhancement by LK-VRR coupling is not large enough to increase the rate to well above the LIGO/VIRGO lower limit, $12 \text{ Gpc}^{-3} \text{ yr}^{-1}$. For the Galactic Center, the LK-VRR-enhanced rate is ~ 100 times lower than the LIGO/VIRGO limit, and for $M_{\bullet} = 10^4 M_{\odot}$, the rate barely reaches $12 \text{ Gpc}^{-3} \text{ yr}^{-1}$.

Keywords: gravitation – black hole physics – Galaxy: center

1. INTRODUCTION

The recent direct detections of gravitational waves from merging black holes (BHs) and neutron stars (NSs) (Abbott et al. 2016a,b, 2017a,b,c,d) have ushered in the era of gravitational wave (GW) astronomy. One of the key astrophysical questions motivated by these observations relates to the formation of BH and NS binaries: the progenitor stars were much larger, so how could they evolve to become compact objects and be driven close enough to each other to coalesce? A number of formation channels have been proposed and investigated, including isolated binary evolution, or other processes in non-isolated binary systems. In the former case, a high-mass stellar binary is driven by common-envelope evolution or non-conservative mass transfer to a short period, i.e., sufficiently short for the binary to merge within a Hubble time due to energy loss by GW radiation (e.g., Tutukov & Yungelson 1973, 1993; Voss & Tauris 2003; Kalogera et al. 2007; Dominik et al. 2012, 2013; Belczynski et al. 2014, 2016, 2017). Alternatively, rapidly rotating stars in tight binaries can be chemically mixed, preventing their merger early in the evolution, and resulting in BH mergers (Mandel & de Mink 2016; Marchant et al. 2016; de Mink & Mandel 2016).

In most ‘isolated’ binary channels, the orbit at the time of merging is expected to be circular. However, channels involving dynamical environments have been proposed, some of which predict the BH binary in the LIGO band to have a residual and non-negligible eccentricity when reaching the

LIGO band, thereby distinguishing themselves from other formation scenarios. With current techniques based on circular GW strain templates, the maximum eccentricity for a source in the LIGO band to be detectable is ≈ 0.1 (Brown & Zimmerman 2010; East et al. 2013; Huerta & Brown 2013; Lower et al. 2018). Dynamical formation channels include isolated triple systems (Silsbee & Tremaine 2017; Antonini et al. 2017b; Liu & Lai 2017, 2018), mergers arising from interactions in dense clusters (e.g., Sigurdsson & Hernquist 1993; Portegies Zwart & McMillan 2000; O’Leary et al. 2006; Ziosi et al. 2014; Rodriguez et al. 2015, 2016; Kimpson et al. 2016; Mapelli 2016; Samsing & Ramirez-Ruiz 2017; Samsing et al. 2017a,b; Samsing 2018; Rodriguez et al. 2018), and binaries in stellar systems dominated by a central massive BH (MBH; Antonini & Perets 2012; Antonini et al. 2014; Prodan et al. 2015; Stephan et al. 2016; Antonini & Rasio 2016; Petrovich & Antonini 2017; Arca-Sedda & Capuzzo-Dolcetta 2017; Arca-Sedda & Gualandris 2018; Hoang et al. 2018; Randall & Xianyu 2018b,a; Gondán et al. 2018). The eccentricity in the LIGO band predicted by these channels ranges widely, between typically $\sim 10^{-6}$ for cluster models (e.g., Rodriguez et al. 2016), $\sim 10^{-3}$ for triple star models (e.g., Antonini et al. 2017b), and ~ 0.1 for galactic nuclei (e.g., Gondán et al. 2018). Note that some of these models also predict very high eccentricities, i.e., much higher than 0.1 (e.g., due to binary-single interactions in globular clusters, Samsing 2018; Rodriguez et al. 2018), which would likely be missed by current detectors.

In the case of binaries dominated by a central massive BH, the torque of the MBH can accelerate the merging process through Lidov-Kozai oscillations (Lidov 1962; Kozai 1962; see Naoz 2016 for a review). The LK dynamics of binaries

around MBHs are complicated by the existence of a large range of physical processes taking place at comparable time-scales such as mass precession, relativistic precession, and processes related to stellar relaxation. These processes depend on the binary separation, the distance of the binary to the MBH, the MBH mass, and the properties of the stellar cluster around the MBH (see, e.g., [Antonini & Perets 2012](#) for an overview).

In most previous studies, the binary+MBH system was treated as an isolated three-body system, and other processes related to relaxation with other stars in the cluster around the MBH were not taken into account directly. Recently, [VanLandingham et al. \(2016\)](#) and [Petrovich & Antonini \(2017\)](#) took the first next step by self-consistently treating effects associated with stellar relaxation on the evolution of the binary+MBH system.

In particular, [Petrovich & Antonini \(2017\)](#) showed that, if the stellar cluster around the MBH is nonspherical, then the associated torques on the binary system around the MBH can give rise to chaotic secular dynamics, resulting in enhanced eccentricity excitation in the binary and increased rates of BH mergers, assuming that the stellar cluster is sufficiently nonspherical. These dynamics are analogous to secular chaotic dynamics in hierarchical quadruple systems, i.e., with an additional fourth body instead of a nonspherical background potential ([Hamers & Lai 2017](#); [Grishin et al. 2018](#)).

In this paper, we focus on a physical process that applies even in the absence of significant nonsphericity of the stellar cluster around the MBH. Close to an MBH (within its sphere of influence), the motion is nearly Keplerian, and encounters between stars are therefore correlated. These correlated encounters give rise to torques that can change both the direction and magnitude of the angular momentum of the orbit of the binary around the MBH (i.e., the ‘outer orbit’), in a process called resonant relaxation (RR; [Rauch & Tremaine 1996](#); [Hopman & Alexander 2006](#); [Eilon et al. 2009](#); [Perets et al. 2009](#); [Merritt et al. 2011](#); [Kocsis & Tremaine 2011](#); [Antonini & Merritt 2013](#); [Bar-Or & Alexander 2014](#); [Hamers et al. 2014](#); [Kocsis & Tremaine 2015](#); [Sridhar & Touma 2016a,b](#); [Bar-Or & Alexander 2016](#); [Fouvry et al. 2017](#); [Bar-Or & Fouvry 2018](#)). The effect of RR on the magnitude of the angular momentum vector is known as scalar RR (SRR), whereas the change of the direction of the angular momentum vector is associated with vector RR (VRR). Both SRR and VRR can be important for the secular binary+MBH evolution. First, a change of the direction of the outer orbital angular momentum vector can induce a mutual inclination between the inner and outer orbits, even if they were initially (close to) coplanar. Subsequently, a mutual inclination can drive high-eccentricity LK oscillations in the inner binary. Second, the torque of the outer binary on the inner binary increases with the outer orbit eccentricity e_{out} , increasing the efficiency (i.e., decreasing the time-scale, see equation 11, and increasing the strength, see equation 13) of the LK mechanism.

The effects of RR on the binary+MBH system were investigated recently by [VanLandingham et al. \(2016\)](#) using a hybrid N -body technique, in which a small stellar cluster (307 to 4400 stars) around a massive object (10^3 to $10^4 M_{\odot}$) was integrated, and its output was used to perturb the binary+MBH system in separate 3-body integrations. Although innovative with this technique and the first to incorporate RR with the binary+MBH evolution, the simulations of [VanLandingham et al. \(2016\)](#) were limited in terms of low particle numbers and low central MBH masses due to computational limitations.

Also, because direct N -body techniques were used, not much insight could be gained into the fundamental dynamics. Here, we adopt a less computationally expensive approach in which the binary+MBH system is integrated with a secular code, and the effects of VRR are incorporated by adopting a simplified model. This approach allows us to more efficiently disentangle the different physical processes; in particular, it allows us to investigate the importance of details of VRR-related dynamics and the impact on the long-term secular evolution of the binary+MBH system. Furthermore, our approach is not limited in terms of MBH mass, and its speed allows for the calculation of a large number of systems to explore larger regions of the parameter space. We note that our focus is on VRR; SRR, although potentially important for the long-term LK evolution of binaries around an MBH, is beyond the scope of this paper.

The plan of the paper is as follows. In Section 2, we give an overview of the time-scales of interest for binaries around MBHs, and identify potential regions of interest for enhanced rates of BH and NS mergers induced by LK-VRR coupling. We describe a model to take into account the effect of VRR on the outer orbit in Section 3. In Section 4, we explore how VRR can affect the LK dynamics of binaries around MBHs. We carry out detailed Monte Carlo calculations including other effects such as post-Newtonian (PN) corrections and binary evaporation, and evaluate the enhancement of merger rates due to LK-VRR coupling in Section 5. We discuss our results in Section 6, and conclude in Section 7.

2. TIME-SCALES

Galactic nuclei with a central MBH are complex dynamical environments, and various physical processes are relevant to the evolution of binaries within these systems. First, we give a brief overview of the important time-scales (similar time-scale calculations can be found in, e.g., Section 3 of [Antonini & Perets 2012](#); for a general overview of galactic nuclei dynamics, we refer to [Merritt 2013](#)). We then compare the various time-scales for different cluster and binary properties, and explore the regimes in parameter space in which LK-VRR coupling could potentially be important for enhancing binary merger rates (a more detailed investigation is carried out in Sections 4 and 5).

An overview of the notation used in this paper is given in Table 1. Throughout, we assume, for simplicity, a spherically symmetric cluster around the MBH with a typical stellar mass $m_{\star} \equiv \langle m^2 \rangle^{1/2}$ (i.e., m_{\star} is the square root of the average of the squared stellar mass in the cluster), and a simple lower-law density distribution, i.e., $\rho_{\star}(r) \propto r^{-\gamma}$. For a Salpeter mass function, $dN/dm \propto m^{-2.35}$, ([Salpeter 1955](#)), and assuming lower and upper mass limits of 0.08 and 80 M_{\odot} , respectively, $\langle m^2 \rangle^{1/2} \approx 1.1 M_{\odot}$. For a top-heavy mass function, $dN/dm \propto m^{-1.7}$, and with the same mass ranges, $\langle m^2 \rangle^{1/2} \approx 5.3 M_{\odot}$. For simplicity, we consider only the case of a Salpeter mass function for the stellar cluster in our simulations, and set $m_{\star} = 1 M_{\odot}$.

2.1. Mass precession

Distributed mass enclosed within an orbit around the MBH causes the orbit to precess in its plane, a process known as mass precession. The time-scale to precess by π is given approximately by (e.g., [Merritt 2013](#), S4.4.1)

$$t_{\text{MP}} \approx \frac{1}{2} (1 - e^2)^{-1/2} \frac{M_{\bullet}}{M_{\star}(a)} P. \quad (1)$$

Symbol	Description
G	Gravitational constant.
c	Speed of light.
Stellar cluster	
r	Distance from the MBH.
M_\bullet	Mass of the MBH.
m_\star	Average background stellar mass.
a	Semimajor axis of an orbit around the MBH.
e	Eccentricity of an orbit around the MBH.
P	Orbital period of an orbit around the MBH.
$n_\star(r)$	Stellar number density, assumed to be $n_\star \propto r^{-\gamma}$.
$\rho_\star(r)$	Stellar mass density, $\rho_\star(r) = m_\star n_\star(r)$.
$\sigma_\star(r)$	One-dimensional stellar velocity dispersion.
$N_\star(a)$	Number of stars within radius $r = a$ from the MBH.
$M_\star(a)$	Mass of stars within radius $r = a$ from the MBH.
\mathbf{J}	Angular-momentum vector of an orbit around the MBH; $J = \sqrt{GM_\bullet a(1-e^2)}$ if the stellar potential is neglected.
J_c	Angular momentum of a circular orbit around the MBH.
γ	Density slope ($\rho_\star \propto r^{-\gamma}$).
Binary+MBH triple system	
M_1	Inner orbit primary mass.
M_2	Inner orbit secondary mass.
a_{in}	Inner orbit semimajor axis.
a_{out}	Outer orbit semimajor axis.
P_{in}	Inner orbital period.
P_{out}	Outer orbital period.
e_{in}	Inner orbit eccentricity.
e_{out}	Outer orbit eccentricity.
\mathbf{e}_{in}	Inner orbit eccentricity vector.
\mathbf{e}_{out}	Outer orbit eccentricity vector.
\mathbf{j}_{in}	Inner orbit normalized angular-momentum vector; its norm is $j_{\text{in}} = \sqrt{1-e_{\text{in}}^2}$.
\mathbf{j}_{out}	Outer orbit normalized angular-momentum vector.
i_{rel}	Relative inclination between the inner and outer orbits ($\cos i_{\text{rel}} = \mathbf{j}_{\text{in}} \cdot \mathbf{j}_{\text{out}}$).
ω_{in}	Inner orbit argument of periapsis.
ω_{out}	Outer orbit argument of periapsis.

Table 1

Description of symbols used throughout this paper.

Mass precession changes the (in-plane) orientation of all orbits around the MBH, which is important for RR (see Section 2.3). In the case of a binary around the MBH, mass precession acts on the outer orbit, and this can potentially quench LK oscillations. However, the quadrupole-order secular MBH+binary equations of motion do not depend on ω_{out} , the outer orbit argument of periapsis. As shown below, in situations where LK-induced mergers can potentially be enhanced due to VRR, the quadrupole-order terms dominate (i.e., the octupole parameter ϵ_{Oct} is small, see also Section 2.6). Therefore, mass precession is not an important quenching source for LK oscillations in our case.

2.2. Relativistic precession

The lowest-order relativistic effect (assuming non-spinning MBHs) is precession of the argument of periapsis of both inner and outer orbits, with time-scales to precess by π given by (Weinberg 1972)

$$t_{1\text{PN},\text{in}} = \frac{1}{6} (1 - e_{\text{in}}^2) \frac{a_{\text{in}} c^2}{G(M_1 + M_2)} P_{\text{in}}; \quad (2a)$$

$$t_{1\text{PN},\text{out}} = \frac{1}{6} (1 - e_{\text{out}}^2) \frac{a_{\text{out}} c^2}{GM_\bullet} P_{\text{out}}. \quad (2b)$$

In equation (2b), we assumed that $M_\bullet \gg M_1, M_2$. Also, we neglect any PN coupling between the inner and outer orbits (Naoz et al. 2013). Relativistic precession in the inner orbit can be an important source of quenching of LK cycles, and this needs to be taken into account. Relativistic precession in the outer orbit is typically unimportant for our purposes, for the same reason discussed in Section 2.1.

2.3. Resonant Relaxation

As mentioned in the Introduction, RR arises from the torques generated on a test orbit by correlated encounters with other stars close to the MBH. One can distinguish between two regimes: the coherent regime, in which the stellar background potential is roughly fixed (in an orbit-averaged sense), and the incoherent regime, in which both in-plane and out-of-plane precession cause the background potential to evolve. In the coherent regime, the (approximately constant) net torque on a test orbit is $\sim \sqrt{N_\star} G m_\star / a$, which leads to a change of the orbital angular momentum

$$\left(\frac{\Delta J}{J_c}\right)_{\text{coh}} \approx \beta \frac{m_\star}{M_\bullet} \sqrt{N_\star} \frac{\Delta t}{P}, \quad (3)$$

where β is a dimensionless number, which can be computed as a function of eccentricity and density slope γ (Kocsis & Tremaine 2015). Here, for simplicity, we set β to $\beta_v = 2$ for VRR. One can define the VRR (or ‘2d RR’, see also Merritt 2013, Section 5.6.1.3) time-scale as the duration for which $\Delta J_{\text{coh}} = J_c$, i.e.,

$$t_{\text{VRR}} \equiv \frac{P M_\bullet}{\beta_v m_\star} \frac{1}{\sqrt{N_\star}}. \quad (4)$$

On time-scales longer than the coherence time-scale t_{coh} , the angular momentum of the test orbit evolves approximately as a random walk with a step size given by the angular momentum-change accumulated during the coherent regime, i.e.,

$$\left(\frac{\Delta J}{J_c}\right)_{\text{incoh}} \approx \left(\frac{\Delta t}{t_{\text{coh}}}\right)^{1/2} \left(\frac{\Delta J}{J_c}\right)_{\text{coh,step}} \equiv \left(\frac{\Delta t}{t_{\text{SRR}}}\right)^{1/2}, \quad (5)$$

where $(\Delta J/J_c)_{\text{coh,step}}$ is equation (3) evaluated at $\Delta t = t_{\text{coh}}$, and where after the second equality we defined the SRR (or ‘3d RR’, see also Merritt 2013, Section 5.6.1.3) time-scale. From equations (3) and (5), it is straightforward to show that

$$t_{\text{SRR}} \equiv \frac{1}{\beta_s^2} \left(\frac{M_\bullet}{m_\star}\right)^2 \frac{1}{N_\star} \frac{P^2}{t_{\text{coh}}}, \quad (6)$$

where we set¹ $\beta_s = 2$. If the reorientation of the (orbit-averaged) stellar background potential arises from mass precession, then $t_{\text{coh}} = t_{\text{MP}}$, and (averaging t_{MP} over a thermal distribution, Jeans 1919)

$$t_{\text{SRR}} = \frac{1}{\beta_s^2} \frac{M_\bullet}{m_\star} P, \quad (7)$$

such that $t_{\text{VRR}} = (\beta_s^2/\beta_v) t_{\text{SRR}} \sqrt{N_\star}$. This shows that $t_{\text{VRR}} < t_{\text{SRR}}$, unless N_\star is small (i.e., very close to the MBH).

¹ Strictly speaking, β_v and β_s are not the same. However, they differ little, e.g., Merritt (2013, S5.6.1.3), and for simplicity we set $\beta_s = \beta_v = 2$ for the purposes of the time-scales shown in Fig. 1.

Coherence of the stellar background is generally broken by relativistic precession or mass precession, whichever process dominates. We write the effective coherence time-scale as

$$t_{\text{coh}}^{-1} = \langle\langle t_{\text{1PN, out}} \rangle\rangle^{-1} + \langle\langle t_{\text{MP}} \rangle\rangle^{-1}, \quad (8)$$

where the double brackets denote averages over e_{out} assuming a thermal distribution.

2.4. Nonresonant relaxation

At larger distances from the MBH, encounters become uncorrelated, and RR becomes ineffective. Uncorrelated encounters give rise to nonresonant relaxation (NRR), which changes all orbital elements of a test orbit on a time-scale given by

$$t_{\text{NRR}} \approx C_{\text{NRR}}(\gamma) \left(\frac{M_{\bullet}}{m_{\star}} \right)^2 \frac{P}{N_{\star} \ln \Lambda}. \quad (9)$$

Here, the NRR time-scale is defined in terms of the angular-momentum diffusion coefficient in the limit of zero angular-momentum; the dimensionless quantity $C_{\text{NRR}}(\gamma)$ is a function of the density slope γ (see Appendix B of [Hamers et al. 2014](#)). For the Coulomb logarithm, we assume $\Lambda = M_{\bullet}/(2m_{\star})$. From equation (9), it is clear that $t_{\text{NRR}} \gg t_{\text{VRR}}$.

2.5. Binary evaporation

Uncorrelated encounters with other stars not only affect the orbital elements of the outer orbit, but also those of the inner orbit ([Binney & Tremaine 2008](#); [Perets 2009](#)). The nature of the effect on the inner orbit semimajor axis depends on the ratio of the (absolute value of the) binding energy, $\mathcal{E}_{\text{in}} = G(M_1 + M_2)/(2a_{\text{in}})$, to the squared stellar velocity dispersion, $\sigma_{\star}^2(r)$ ([Heggie 1975](#)). If the inner binary is soft, $G(M_1 + M_2)/(2a_{\text{in}}) \ll \sigma_{\star}^2$, then encounters tend to make it even softer (a_{in} increases), whereas hard binaries, for which $G(M_1 + M_2)/(2a_{\text{in}}) \gg \sigma_{\star}^2$, tend to become harder (a_{in} decreases; e.g., [Hut 1993](#); [Heggie et al. 1996](#)).

For soft binaries, the time-scale for the inner orbit binding energy to change by order itself is given by ([Alexander & Pfuhl 2014](#))

$$t_{\text{EV}} = \frac{1}{8} \sqrt{\frac{1 + q_{\sigma}}{2\pi q_{\sigma}}} \frac{M_1 + M_2}{m_{\star}} \frac{\sigma_{\star}(r)}{G n_{\star}(r) m_{\star} a_{\text{in}} \ln \Lambda_{\text{in}}}, \quad (10)$$

where $q_{\sigma} \equiv (M_1 + M_2)/m_{\star}$, and $\Lambda_{\text{in}} = 3(1 + 1/q_{\sigma})/(1 + 2/q_{\sigma})[\sigma_{\star}^2(r)/v_{\text{in}}^2]$, with $v_{\text{in}}^2 = G(M_1 + M_2)/a_{\text{in}}$ ([Alexander & Pfuhl 2014](#)).

2.6. LK cycles

The quadrupole-order time-scale of LK oscillations can be estimated as (e.g., [Innanen et al. 1997](#); [Kinoshita & Nakai 1999](#); [Antognini 2015](#))

$$t_{\text{LK}} = \frac{8}{15\pi} \left(\frac{P_{\text{out}}^2}{P_{\text{in}}} \right) \frac{M_1 + M_2 + M_{\bullet}}{M_{\bullet}} (1 - e_{\text{out}}^2)^{3/2}. \quad (11)$$

We shall refer to the ratio of the LK and VRR time-scales as the ‘adiabatic parameter’ \mathcal{R} ,

$$\begin{aligned} \mathcal{R} &\equiv \frac{t_{\text{LK}}}{t_{\text{VRR}}} = \frac{8}{15\pi} \frac{P_{\text{out}}}{P_{\text{in}}} \frac{M_1 + M_2 + M_{\bullet}}{M_{\bullet}} \frac{m_{\star}}{M_{\bullet}} \beta_{\text{v}} \sqrt{N_{\star}} (1 - e_{\text{out}}^2)^{3/2} \\ &\simeq \frac{8}{15\pi} \left(\frac{a_{\text{out}}}{a_{\text{in}}} \right)^{3/2} \left(\frac{M_1 + M_2}{M_{\bullet}} \right)^{1/2} \frac{m_{\star}}{M_{\bullet}} \beta_{\text{v}} \sqrt{N_{\star}} (1 - e_{\text{out}}^2)^{3/2}, \end{aligned} \quad (12)$$

where in the last line we assumed $M_{\bullet} \gg M_1, M_2$. One can consider $\mathcal{R} \ll 1$ to be the ‘adiabatic’ regime in which VRR slowly changes the orientation of the outer orbit, and on time-scales $\ll t_{\text{VRR}}$, the system is well described as an isolated three-body system. Non-adiabatic regimes ($\mathcal{R} \sim 1$ or $\mathcal{R} \gg 1$) are associated with different behavior, and we consider these regimes in more detail in Section 4.

The importance of the octupole-order terms can be estimated by the octupole parameter ϵ_{oct} (which is essentially the ratio of the coefficient of the octupole-order term to the coefficient of the quadrupole-order term),

$$\epsilon_{\text{oct}} \equiv \frac{|M_1 - M_2|}{M_1 + M_2} \frac{a_{\text{in}}}{a_{\text{out}}} \frac{e_{\text{out}}}{1 - e_{\text{out}}^2}. \quad (13)$$

Orbital flips, and associated high eccentricities, can occur if $\epsilon_{\text{oct}} \gtrsim 10^{-3}$ ([Lithwick & Naoz 2011](#); [Katz et al. 2011](#); [Teyssandier et al. 2013](#); [Li et al. 2014](#)). We evaluate typical values of ϵ_{oct} for our systems of interest below.

2.7. Comparison of times-scales for different parameters

We compute the various time-scales discussed above for clusters with different M_{\bullet} and γ , and for different inner binary semimajor axes a_{in} . We set the inner binary masses to $M_1 = 30 M_{\odot}$ and $M_2 = 20 M_{\odot}$, representing some of the recent LIGO systems, and the outer orbit eccentricity is set to $e_{\text{out}} = 2/3$ (the mean value for a thermal distribution, [Jeans 1919](#)). The inner orbit eccentricity, used to calculate $t_{\text{1PN, in}}$, is set to $e_{\text{in}} = 0$ (an optimistic assumption in terms of quenching of LK oscillations). The average background stellar mass is set to $m_{\star} = 1 M_{\odot}$.

To set the overall normalization of the stellar distribution, we adopt the $M_{\bullet} - \sigma_{\text{bulge}}$ -relation between the MBH mass and bulge velocity dispersion σ_{bulge} ([Merritt & Ferrarese 2001](#)),

$$\log_{10} \left(\frac{M_{\bullet}}{M_{\odot}} \right) = 4.8 \log_{10} \left(\frac{\sigma_{\text{bulge}}}{\text{km s}^{-1}} \right) - 2.9, \quad (14)$$

and set σ_{bulge} to $\sigma_{\star}(r_{\text{h}})$, where r_{h} is the radius at which the enclosed distributed stellar mass is $2M_{\bullet}$ (i.e., combining two definitions for the radius of influence).

Specifically, assuming a spherically symmetric stellar number density distribution $n_{\star}(r) = n_{\text{h}}(r/r_{\text{h}})^{-\gamma}$ and using the isotropic Jeans equation, one can show that r_{h} and σ_{\star} , where σ_{\star} is the velocity dispersion at $r = r_{\text{h}}$, are related via

$$r_{\text{h}} = \frac{GM_{\bullet}}{\sigma_{\star}^2} \frac{1}{1 + \gamma} \left(1 + \frac{1 + \gamma}{\gamma - 1} \right). \quad (15)$$

For a given M_{\bullet} and γ , we compute σ_{bulge} from the $M_{\bullet} - \sigma_{\text{bulge}}$ -relation ([Merritt & Ferrarese 2001](#)), set $\sigma_{\star} = \sigma_{\text{bulge}}$, and calculate r_{h} from equation (15). The normalization n_{h} is then given by $n_{\text{h}} = [(3 - \gamma)/(4\pi)](2M_{\bullet}/m_{\star})r_{\text{h}}^{-3}$. Related quantities such as N_{\star} and M_{\star} are found by straightforward integration over volume of $n_{\star}(r)$.

We show the resulting time-scales and ϵ_{oct} as a function of r , normalized by r_{h} , in Fig. 1. Each panel corresponds to a different combination of M_{\bullet} , γ and a_{in} . Refer to the legends and/or the figure caption for the meaning of the various colors and line styles.

The regions of interest are where the LK and VRR time-scales are similar, and a number of other conditions are met. In Fig. 1, we highlight with thick solid dark red lines the radii for which

- (i) $0.1 < \mathcal{R} < 10$;

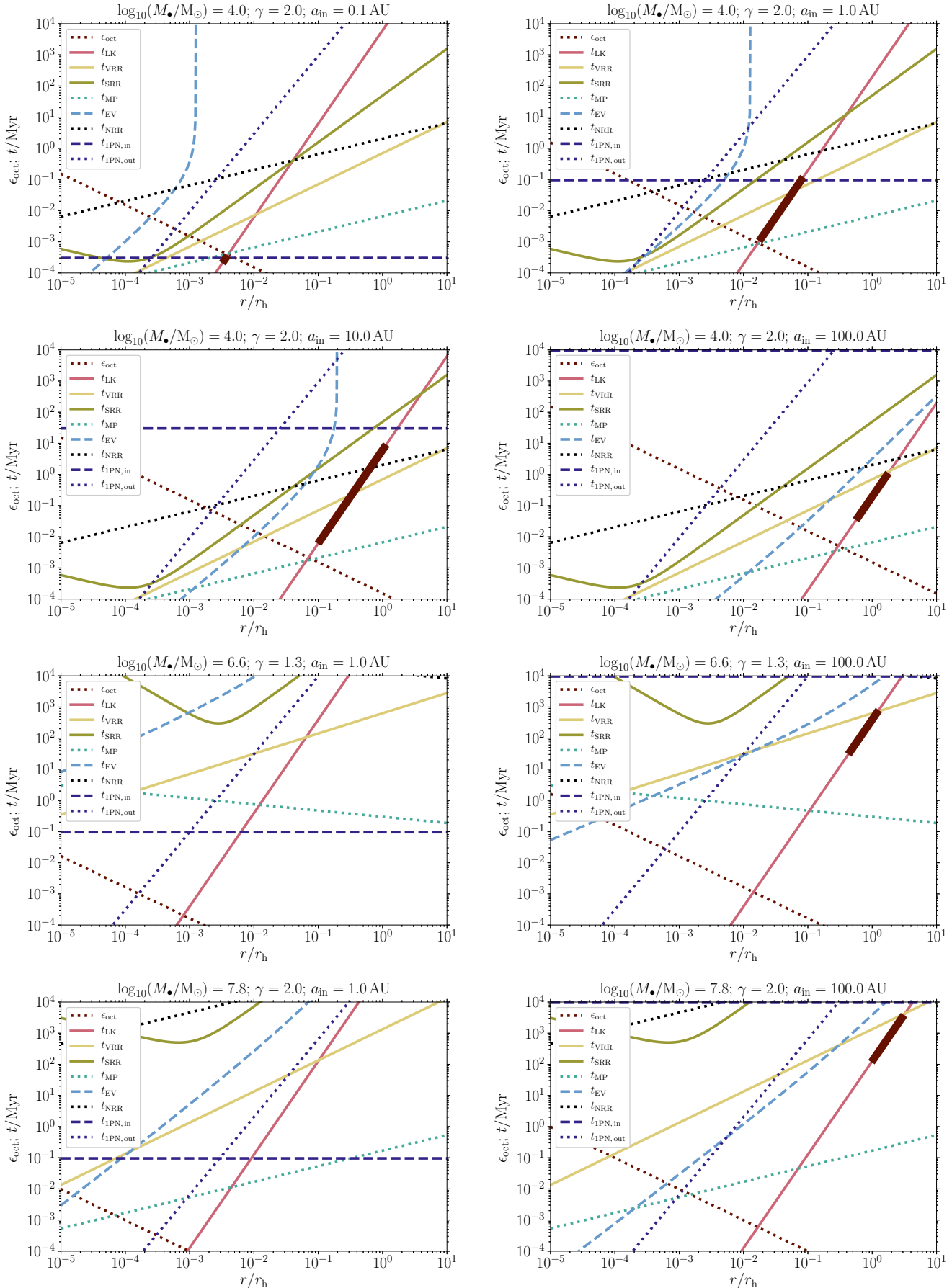


Figure 1. Various time-scales and octupole parameter as a function of distance to the MBH, r , normalized to r_h . The octupole parameter (equation 13) is shown with the dark red dotted line. Other lines show various time-scales: t_{LK} : red solid; t_{VRR} : light yellow solid; t_{SRR} : dark yellow solid; t_{MP} : light green dotted; t_{EV} : light blue dashed; t_{NRR} : black dotted; $t_{IPN,in}$: dark blue dashed (setting $e_{in} = 0$); $t_{IPN,out}$: dark blue dotted. Each panel corresponds to certain values of M_* , γ , and a_{in} , indicated in the top. The thick solid dark red lines indicate the radii for which we expect VRR to be important (not applicable in all panels).

- (ii) $t_{\text{LK}} < t_{\text{EV}}/10$;
- (iii) $t_{\text{LK}} < 10 \text{ Gyr}$;
- (iv) $t_{\text{LK}} < t_{\text{IPN, in}}$.

The chosen range for \mathcal{R} in condition (i) is somewhat arbitrary. We investigate the dynamics as a function of \mathcal{R} in more detail in Section 4. Here, the main aim is to broadly explore the parameter space and pinpoint regions of interest, rather than to accurately capture the dynamics. Condition (ii) ensures that at least $O(10)$ LK cycles occur before the binary evaporates. Condition (iii) excludes LK time-scales that are too long compared to the age of the Universe, and condition (iv) excludes systems in which LK cycles are suppressed by relativistic precession in the inner orbit.

We note the following:

- There are no regions of interest for tight binaries ($a_{\text{in}} = 0.1 \text{ AU}$). This can be ascribed to the short relativistic precession time-scale.
- The kink as a function of r in the SRR time-scale is due to a change of IPN precession being the dominant reshuffling process close to the MBH, to mass precession further away (see equation 8).
- SRR can be as important as VRR close to the MBH, but the regions of interest are located further from the MBH, where $t_{\text{SRR}} \gg t_{\text{VRR}}$.
- The effect of binary evaporation is weak for the regions of interest.
- The NRR time-scale is typically longer than the LK and VRR time-scales in the regions of interest, although there are some cases in which they are comparable (in particular, for low MBH masses and large a_{in}).
- In the regions of interest, the octupole parameter is typically small ($\epsilon_{\text{oct}} \lesssim 10^{-4}$), indicating that the eccentric LK mechanism is expected to be unimportant. Nevertheless, we include the octupole (and higher-order) terms in the numerical integrations in Sections 4 and 5 (see also Section 3.2).

2.8. Potentially interesting regimes

Although Fig. 1 contains detailed information on the time-scales, it is difficult to obtain insight into the dependence of the size of the parameter space of interest as a function of M_{\bullet} , γ and a_{in} . For that purpose, we here determine the number of stars within the radial extent of interest, normalized to the total number of stars. We consider ranges in r between 10^{-5} and $10 r_{\text{h}}$.

Specifically, let r_{in} and r_{out} denote the inner and outer edges of the region for which the criteria discussed in Section 2.7 are satisfied (i.e., the radial region indicated with the thick solid dark red lines in Fig. 1). The number of stars within the region of interest is then $N_{\text{interest}} = N_{\star}(r_{\text{out}}) - N_{\star}(r_{\text{in}})$; the total number of stars is $N_{\text{tot}} = N_{\star}(10 r_{\text{h}})$. Evidently, N_{interest} does not give the actual number of *binaries* of interest; to get the latter number, one should multiply by the binary fraction. We emphasize that $N_{\text{interest}}/N_{\text{tot}}$ does not contain direct information on the enhancement of merger rates due to VRR; it measures the importance of the parameter space for which LK-VRR coupling is potentially important.

In Fig. 2, we show $N_{\text{interest}}/N_{\text{tot}}$ as a function of M_{\bullet} for several values of a_{in} and γ (top four panels), and as a function of a_{in} for several values of M_{\bullet} and γ (bottom four panels). To illustrate the importance of relativistic precession in the inner binary, we show results with (solid lines) and without (dashed lines) the inclusion of criterion (iv) described in Section 2.7.

From Fig. 2, it is clear that there is a strong dependence of $N_{\text{interest}}/N_{\text{tot}}$ on all three parameters M_{\bullet} , γ and a_{in} . Generally, the number fraction is significant (i.e., $\gtrsim 0.04$) for a relatively narrow range of a_{in} , which can be understood by noting that relativistic precession dominates in tight binaries, whereas evaporation and the age of the Universe restrict the region of interest for wide binaries. More massive MBHs imply longer VRR time-scales whereas the LK time-scale decreases. Therefore, $N_{\text{interest}}/N_{\text{tot}}$ decreases for large values of M_{\bullet} .

We investigate the dependence of the importance of LK-VRR coupling and merger rates on the parameters in more detail in Section 5.

3. METHODOLOGY

3.1. Model for Vector Resonant Relaxation

In order to mimic the stochastic motion of the outer orbit by VRR, we construct a toy model which, statistically, reproduces the orbital evolution of a test star due to the stochastic torques of the background. This toy model is based on the assumption that the two important properties of the

stochastic torques are the rms of the torque $\tau_v = J \sqrt{\langle \dot{\mathbf{J}} \cdot \dot{\mathbf{J}} \rangle} = \beta_v \sqrt{N_{\star}} m_{\star} J_c^2 / (M_{\bullet} P)$ and the time scale on which this torque remains coherent t_{coh}^v , which is set by the VRR timescale, $t_{\text{coh}}^v = \epsilon_c t_{\text{VRR}}$. The free parameter β_v , which determines the magnitude of the torque, can be calculated directly (e.g., Kocsis & Tremaine 2015). To determine ϵ_c , which sets the coherence timescale, we fit the orbital evolution in our toy model to numerical simulations.

We assume that the motion of a test orbit is governed by the quadruple moment of the background stars. The evolution of the angular-momentum vector is given by the equation of motion

$$\dot{\mathbf{J}} = J^{-1} \tau_v(Q(t)\hat{\mathbf{J}}) \times \hat{\mathbf{J}}, \quad (16)$$

where $Q(t)$ is a time dependent matrix

$$Q = \sqrt{\frac{3}{4}} \begin{pmatrix} \eta_{2r}(t) & \eta_{2i}(t) & -\eta_{1r}(t) \\ \eta_{2i}(t) & -\eta_{2r}(t) & -\eta_{1i}(t) \\ -\eta_{1r}(t) & -\eta_{1i}(t) & \sqrt{3}\eta_0(t) \end{pmatrix}, \quad (17)$$

which depends on the intricate motion of the background stars through its decomposition into spherical harmonics $\eta_{ir}(t) \propto \sum_n \Re[Y_{2i}(\hat{\mathbf{J}}_n(t))]$, $\eta_{ii}(t) \propto \sum_n \Im[Y_{2i}(\hat{\mathbf{J}}_n(t))]$, where $(\hat{\mathbf{J}}_n(t))$ are angular momentum vectors of background stars. This model has two free parameters, β_v and ϵ_c , which determine the magnitude of the torque and the coherence time, respectively.

Instead of following the complex motion of the background, we replace the $\eta_i(t) \in \{\eta_0, \eta_{1r}(t), \eta_{1i}(t), \eta_{2r}(t), \eta_{2i}(t)\}$ functions by Gaussian noise terms with similar statistical properties as the exact ones.

These noise terms are of zero mean $\langle \eta_i(t) \rangle = 0$, and are fully described by their correlation function $\langle \eta_i(t) \eta_j(t') \rangle = \delta_{ij} C(t - t')$, which is normalized such that $\langle \dot{\mathbf{J}} \cdot \dot{\mathbf{J}} \rangle = \tau_v^2$. The coherence time, which is the timescale on

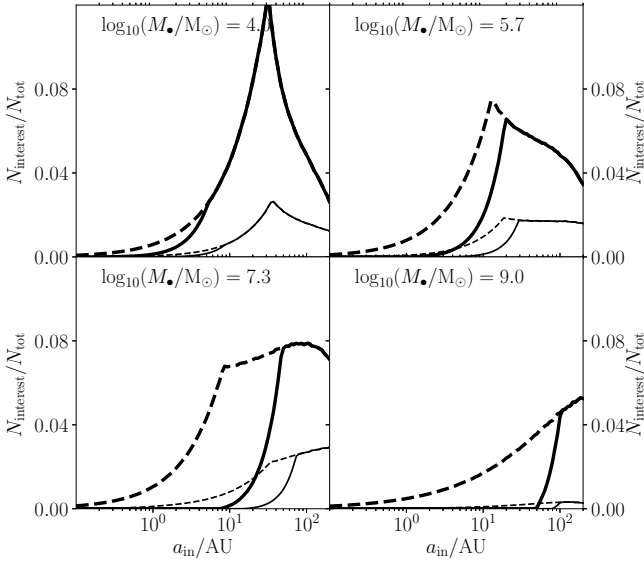
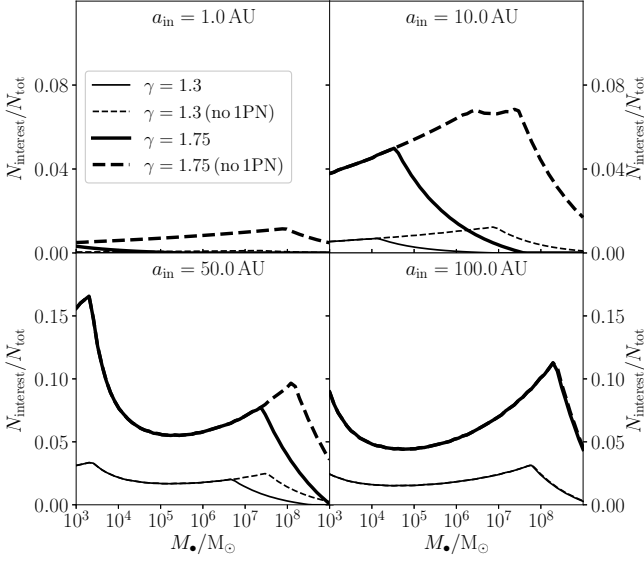


Figure 2. Number of stars within the region of interest, N_{interest} , normalized to the total number of stars, N_{tot} (see text in Section 2.8). The region of interest is defined with the criteria in Section 2.7. The ratios $N_{\text{interest}}/N_{\text{tot}}$ are shown as a function of M_* for several values of a_{in} and γ (top four panels), and as a function of a_{in} for several values of M_* and γ (bottom four panels). Solid (dashed) lines show $N_{\text{interest}}/N_{\text{tot}}$ with (without) taking into relativistic precession in the inner orbit.

which $C(t - t')$ decays, is set by fitting the correlation in $\hat{\mathbf{J}}$ to effective N -body simulations.

Here, we implement correlated noise with a correlation timescale t_{coh}^v , by drawing η_j^i from a Gaussian distribution, with zero mean and standard deviation of 1, at times t_i each coherence time $t_{i+1} - t_i = t_{\text{coh}}^v$, and linearly interpolating between η_j^i and η_j^{i+1} . Thus, on the interval $t_i \leq t < t_{i+1}$, the noise

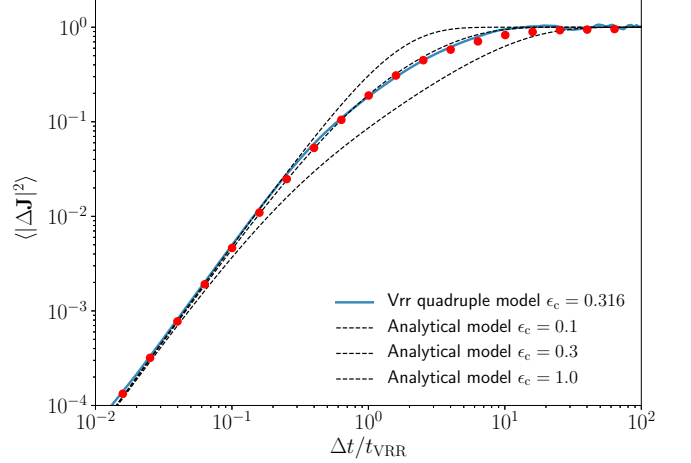


Figure 3. Change in the direction of the angular-momentum of the outer orbit $\langle (\Delta \hat{\mathbf{J}})^2 \rangle$ as a function of time for the VRR model (solid blue line) fitted to the data from numerical simulations of interacting rings (red dots). For reference, the black dashed lines show the analytic approximation in equation (21) with different values of ϵ_c .

terms are given by

$$\eta_j(t) = \eta_j^i + (\eta_j^{i+1} - \eta_j^i)(t - t_i)/t_{\text{coh}}^v, \quad (18)$$

and the correlation function is

$$C(t) = \begin{cases} \frac{2}{3} + \frac{t - 2t_{\text{coh}}^v}{2(t_{\text{coh}}^v)^3} t^2, & |t| \leq t_{\text{coh}}^v; \\ \frac{(2t_{\text{coh}}^v - |t|)^3}{6(t_{\text{coh}}^v)^3}, & t_{\text{coh}}^v < |t| \leq 2t_{\text{coh}}^v; \\ 0, & |t| > 2t_{\text{coh}}^v. \end{cases} \quad (19)$$

To compare this scheme to numerical simulations, we define the mean squared change in orientation of the angular momentum over time $\Delta t = t' - t$ as

$$\langle (\Delta \hat{\mathbf{J}})^2 \rangle \equiv \frac{1}{2} \langle |\hat{\mathbf{J}}(t) - \hat{\mathbf{J}}(t')|^2 \rangle = 1 - \langle \hat{\mathbf{J}}(t) \cdot \hat{\mathbf{J}}(t') \rangle. \quad (20)$$

On short timescales, $t \ll t_{\text{coh}}^v$, the torque is nearly constant and the evolution of $\hat{\mathbf{J}}$ is ballistic $\langle (\Delta \hat{\mathbf{J}})^2 \rangle \approx \tau_v t^2 / (2J)$. On long timescales, $t \gg t_{\text{coh}}^v$, the torque is reshuffled and $\hat{\mathbf{J}}$ changes in a diffusive manner $\langle (\Delta \hat{\mathbf{J}})^2 \rangle \approx 1 - \exp(-D_{\text{VRR}} t)$, where $D_{\text{VRR}} = J^{-2} \tau_v^2 (t_{\text{coh}}^v)^2$ is the diffusion coefficient.

We verified our model for VRR by carrying out a number of integrations of the equations of motion (without the terms accounting for the secular binary+MBH interaction), and by comparing the evolution of $\hat{\mathbf{J}}$ to numerical simulations of interacting rings. In these simulations, we used a set of gravitationally interacting circular rings and advanced the system by calculating the mutual torques between all ring-pairs at each time-step (see, e.g., [Ulubay-Siddiki et al. 2009](#)). As shown in Fig 3, $\langle (\Delta \hat{\mathbf{J}})^2 \rangle$ can be analytically approximated by

$$\langle \hat{\mathbf{J}}(0) \cdot \hat{\mathbf{J}}(t) \rangle \approx 1 - \exp[-J^{-2} \tau_v^2 (t_{\text{coh}}^v)^2 \chi(t/t_{\text{coh}}^v)], \quad (21)$$

where $\chi(x) = x - 1 + \exp(-x)$, and the model is consistent with the ring simulations, for $\epsilon_c \approx 0.316$.

3.2. Secular dynamics

To describe the secular dynamics of the binary+MBH system, we adopt the standard equations of motion for hierarchical triple systems based on an expansion of the Hamiltonian in terms of the ratio of the separations of the inner and outer orbits. The Hamiltonian is averaged over both orbits, and the equations of motion (in vector form) are integrated numerically. By default, we include the quadrupole, octupole, hexadecapole and dotriacontupole-order terms as implemented within SECULARMULTIPLE (Hamers & Portegies Zwart 2016), in which we have included the VRR model described in Section 3.1. Although not studied here, the implementation also supports the inclusion of VRR on the orbits of more complicated subsystems orbiting the MBH, e.g., multiplanet systems within binaries.

4. UNDERSTANDING THE DYNAMICS

In this section, we address in detail the impact of VRR on the LK evolution of the binary+MBH system. We consider the VRR and LK dynamics only, i.e., we include the LK equations of motion and the effects of VRR on the outer orbit. Other physical processes such as PN corrections and binary evaporation are ignored here, but are included in the Monte Carlo integrations in Section 5.

4.1. Illustration of the different regimes

We first show a number of examples to illustrate the dependence of the typical dynamical behavior on the adiabatic parameter \mathcal{R} . In these examples, we fix $e_{\text{out}} = 2/3$. In the limit that \mathcal{R} is very small, i.e., $t_{\text{LK}} \ll t_{\text{VRR}}$, VRR is unimportant, and, to quadrupole order in the test particle approximation, the maximum eccentricity, assuming zero initial eccentricity, is given by the canonical relation

$$e_{\text{in,max}} = \sqrt{1 - \frac{5}{3} \cos^2(i_{\text{rel},0})}, \quad (22)$$

where $i_{\text{rel},0}$ is the initial mutual inclination. If \mathcal{R} is larger, in particular, $\mathcal{R} \sim 1$, significant eccentricity excitation is possible even if the initial mutual inclination is small, including coplanar configurations. This is illustrated in Figures 4 and 5, in which $\mathcal{R} \simeq 0.11$ and $\simeq 1.3$, respectively. In these examples, there is significant eccentricity excitation, much more than implied by equation (22). In particular, in Fig. 5, the initial mutual inclination is $i_{\text{rel},0} \approx 30^\circ$, and there would be no eccentricity excitation in the absence of VRR. If VRR is taken into account (with $\mathcal{R} \simeq 1.3$), the mutual inclination changes due to the changing direction of \mathbf{j}_{out} . After a few t_{LK} , i_{rel} increases to 90° , and the eccentricity is excited through a LK-like process. Subsequent eccentricity excitations are associated with inclinations close to 90° , and particularly with orbital flips (changes from prograde to retrograde orbits, and vice versa). For example, a spike in the eccentricity with $1 - e_{\text{in}}$ reaching $\sim 10^{-6}$ occurs after $\approx 90 t_{\text{LK}}$, and which is associated with an orbital flip. Typically, the evolution is complex and chaotic in this regime. High eccentricities are possible even for $\mathcal{R} \simeq 0.1$, as shown in Fig. 4.

In Fig. 6, we illustrate the regime $\mathcal{R} \gg 1$ ($\mathcal{R} = 100$). One might expect that eccentricity excitation is completely suppressed if $t_{\text{LK}} \gg t_{\text{VRR}}$, since the mutual inclination is varying on a short time-scale compared to t_{LK} (see the bottom panel in Fig. 5). Initially, this is the case in Fig. 6, but after several tens of t_{LK} , the eccentricity grows gradually. The evolution in this regime can be characterized as a diffusive process, in

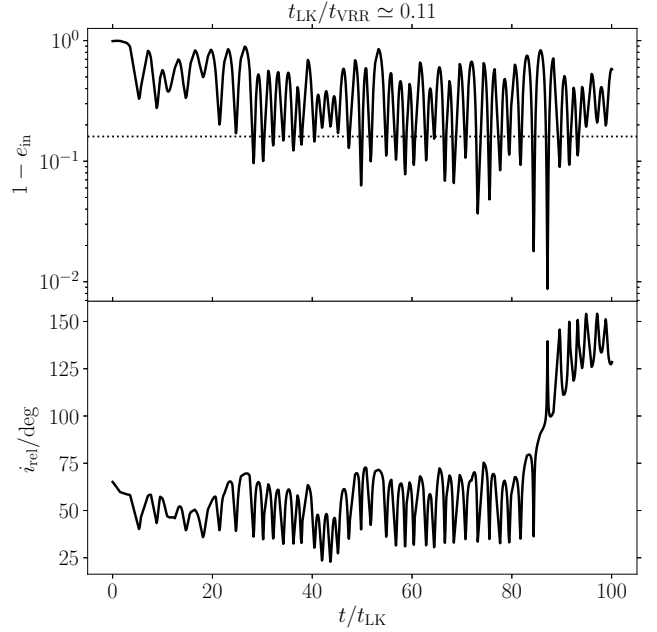


Figure 4. Example evolution in the ‘mildly transadiabatic’ regime, $\mathcal{R} \simeq 0.11$. Top panel: inner orbit eccentricity; bottom panel: mutual inclination between the inner and outer orbits. The initial mutual inclination is $i_{\text{rel},0} \simeq 65^\circ$, and in the canonical case without VRR, the maximum eccentricity (see equation 22) is $\simeq 0.84$ (horizontal dotted line in the top panel). With VRR included, high-eccentricity oscillations occur as a consequence of LK-like evolution induced by high mutual inclinations triggered by VRR. In particular, a flip from prograde to retrograde orientation occurs after $\approx 85 t_{\text{LK}}$. This flip is associated with a maximum eccentricity of $\simeq 0.99$, much larger than $\simeq 0.84$ in the case without VRR.

which the eccentricity grows in a random walk-like fashion with a step size given by $\Delta e_{\text{step}} \sim t_{\text{VRR}}/t_{\text{LK}} = \mathcal{R}^{-1}$. The eccentricity then grows as $\Delta e = \Delta e_{\text{step}}(\Delta t/t_{\text{VRR}})^{1/2}$, implying that e increases to order unity on a time-scale given by (setting $\Delta e = 1$ for $\Delta t = t_{\text{dif}}$)

$$t_{\text{dif}} \sim \mathcal{R}^2 t_{\text{VRR}} = \mathcal{R} t_{\text{LK}}. \quad (23)$$

In Fig. 6, $\mathcal{R} = 100$, and the eccentricity indeed grows to order unity on a time-scale of the order of $\mathcal{R} t_{\text{LK}} = 100 t_{\text{LK}}$.

4.2. Eccentricity distributions as a function of the adiabatic parameter

We investigate the different regimes more quantitatively by carrying out numerical integrations of the equations of motion for different adiabatic parameters, again only including the secular Newtonian three-body terms and VRR. Specifically, for a given value of the adiabatic parameter \mathcal{R} in a range of up to $\mathcal{R} = 100$, we sample 1000 systems with different random orientations of the inner binary with respect to the MBH, and integrate for a duration of $100 t_{\text{LK}}$. Note that, by definition, an elapsed time of t_{LK} corresponds to $\mathcal{R} t_{\text{VRR}}$, i.e., in the longest integration ($\mathcal{R} = 100$) we integrate for $10^4 t_{\text{VRR}}$. For each system, we record the maximum eccentricity reached in the inner orbit, $e_{\text{in,max}}$, by means of root finding (i.e., we search for all local maxima in the integrations, $de_{\text{in}}/dt = 0$, using root finding, and determine from the local maxima the global maximum; this method ensures that there is no risk of missing

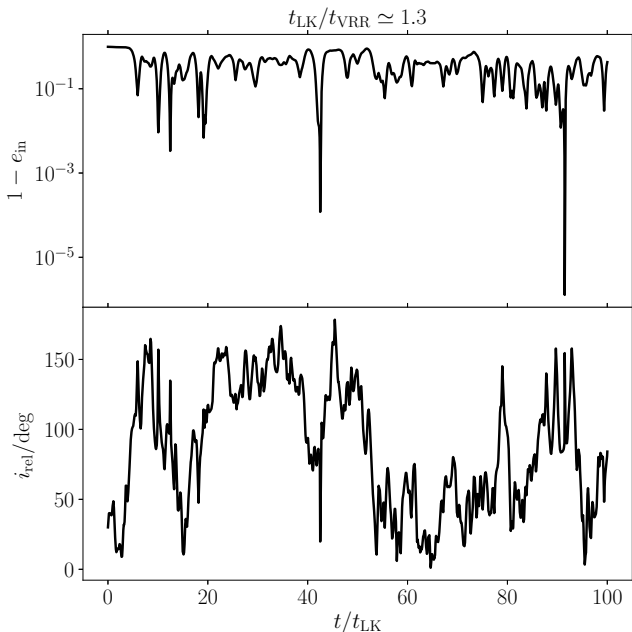


Figure 5. Example evolution in the ‘transadiabatic’ regime, $\mathcal{R} \approx 1.3$. Top panel: inner orbit eccentricity; bottom panel: mutual inclination between the inner and outer orbits. The initial mutual inclination is $i_{\text{rel},0} \approx 30^\circ$, implying no excitation in the case without VRR, yet with VRR, high-eccentricity oscillations occur, reaching values as high as $1 - 10^{-6}$.

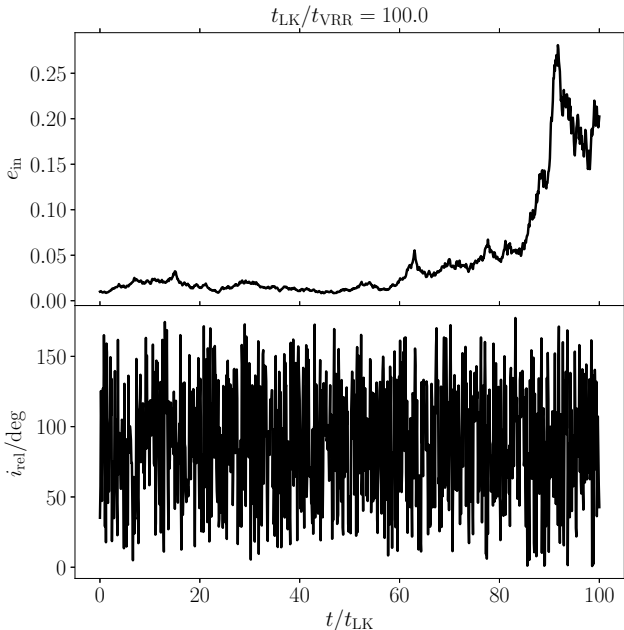


Figure 6. Similar to Fig. 5, now showing example evolution in the regime $\mathcal{R} \gg 1$ ($\mathcal{R} = 100$). Initially, eccentricity excitation is suppressed, but the eccentricity grows slowly in a diffusive process.

the true maximum eccentricity because of a finite number of output snapshots). For simplicity, we fix $e_{\text{out}} = 2/3$.

The resulting cumulative distributions of $e_{\text{in,max}}$ (each based on 1000 simulations) are shown in Fig. 7. Each panel corresponds to a different integration time, indicated in the top. Different lines correspond to different values of \mathcal{R} , indicated in the legend. The black solid line shows the analytic result that applies in the limit $\mathcal{R} = 0$ (i.e., the canonical LK limit without VRR). In that case, it is straightforward to show that

$$N(< j_{\text{in}}) = \sqrt{3/5} j_{\text{in}}, \quad (24)$$

where $j_{\text{in}} = \sqrt{1 - e_{\text{in}}^2}$. The solid dark blue lines in Fig. 7 corresponds to the numerical integrations with $\mathcal{R} = 0$, and agree with the analytical prediction (note that the noise level is at a CDF value of $\sim 1/\sqrt{1000} \approx 0.03$). We identify the following features.

- Already for relatively small \mathcal{R} ($\mathcal{R} \approx 0.03$), there is a significant enhancement in the maximum eccentricity compared to equation (24). For example, after $100 t_{\text{LK}}$ and for $1 - e_{\text{in,max}} = 10^{-4}$, the cumulative fraction is $\sim 10^{-2}$ in the case $\mathcal{R} = 0$, whereas for $\mathcal{R} \approx 0.03$, the cumulative fraction at $1 - e_{\text{in,max}} = 10^{-4}$ is $\sim 10^{-1}$.
- Generally, there is a dependence of the distribution of $e_{\text{in,max}}$ on time. As \mathcal{R} is closer to unity, the dependence becomes weaker, i.e., there is less evolution in the distributions between 20 and $100 t_{\text{LK}}$.
- For a range of \mathcal{R} , $0.1 \lesssim \mathcal{R} \lesssim 10$, the distribution of $e_{\text{in,max}}$ is approximately independent of \mathcal{R} . Related to the above point, the time evolution of this distribution is relatively weak compared to other values of \mathcal{R} . After $100 t_{\text{LK}}$, at $1 - e_{\text{in,max}} = 10^{-4}$ the cumulative fraction for these values of \mathcal{R} is ~ 0.6 , compared to $\sim 10^{-2}$ for the case without VRR.
- For large values of \mathcal{R} , $\mathcal{R} \gtrsim 10$, there is a suppression of maximum eccentricities compared to equation (24) at early times. At later times, the distributions shift significantly to larger eccentricities. After $100 t_{\text{LK}}$ and for $\mathcal{R} = 100$, the median $e_{\text{in,max}}$ is comparable to the case $\mathcal{R} = 0$, but there is a tail towards very high eccentricities which extends to about one order of magnitude in the cumulative fraction at $1 - e_{\text{in,max}} \sim 10^{-5}$. This can be ascribed to the diffusive evolution mentioned previously in Section 4.1.

5. MONTE CARLO SIMULATIONS

In addition to the scale-free integrations of Section 4, we carry out Monte Carlo simulations of BH-BH binaries around MBHs in which we include more (astro)physical effects. In particular, we include PN terms (1PN terms in the inner and outer orbits, and 2.5PN and spin-orbit coupling terms in the inner orbit), Newtonian mass precession terms for the outer orbit, and take into account binary evaporation (with a simplified method, i.e., by limiting the integration time).

5.1. Setup

5.1.1. Initial conditions

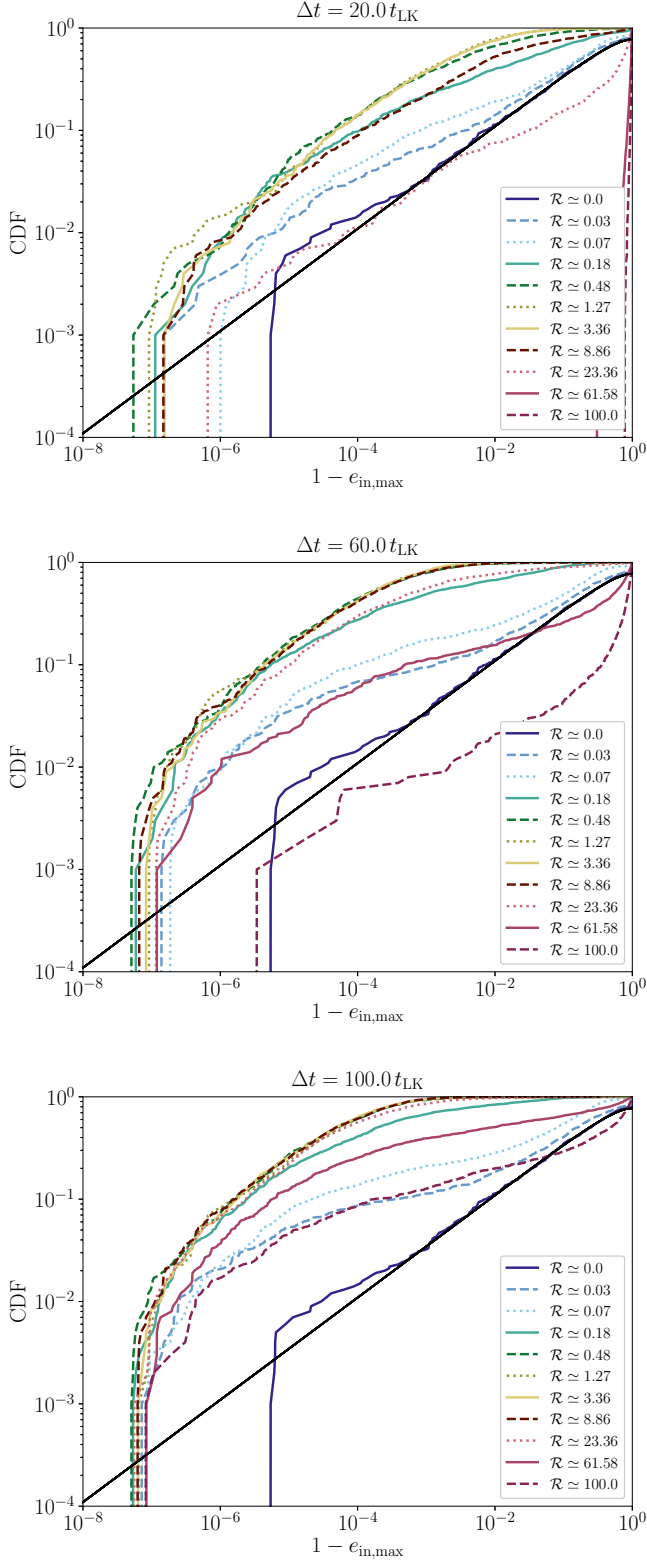


Figure 7. Cumulative distributions of $e_{\text{in,max}}$ (based on 1000 simulations). Each panel corresponds to a different integration time, indicated in the top. Different lines correspond to different values of \mathcal{R} , indicated in the legend. Black solid line: analytic distribution that applies in the limit $\mathcal{R} = 0$ (see equation 24).

We carry out various sets of simulations, each in which we consider the MBH mass and density slope γ to be fixed parameters. For a given M_\bullet and γ , we first calculate the radius of the sphere of influence, r_h , using the same method of Section 2.7, i.e., we assume a stellar density distribution $n_\star(r) = n_h(r/r_h)^{-\gamma}$, and normalize the distribution using the M_\bullet - σ_{bulge} -relation.

The initial distributions of compact object binaries in galactic nuclei are not constrained. Here, we assume simple distributions that do not impose strong biases on the parameters. We emphasize that our assumptions on the distributions are not realistic, and are chosen for simplicity and generality, rather than for realism. A posteriori, our merger rates can be scaled accordingly to more specific distributions.

We generate N_{MC} systems with the following assumptions. First, we sample the primary mass M_1 from a flat distribution with $10 < M_1/M_\odot < 50$, approximately capturing the low-mass range of BHs, and also including the possibility of more massive BHs (the highest BH mass detected by LIGO to date is $\approx 35 M_\odot$ for GW150914, Abbott et al. 2016b). We note that we find few mergers with primary masses lower than 10 and higher than 50 M_\odot . The secondary mass is sampled assuming a flat distribution of the mass ratio $q \equiv M_2/M_1$, with a minimum secondary mass of $M_2 = 10 M_\odot$. A flat mass ratio distribution is appropriate for massive (main-sequence) stars (Sana et al. 2012; Duchêne & Kraus 2013; Kobulnicky et al. 2014), although it likely does not apply to compact object binaries. We note, however, that there is no discernible preference for mergers regarding q , as shown below.

The inner and outer semimajor axes are sampled from a flat distribution in $\log_{10}(a_i/\text{AU})$ (i.e., Öpik’s law, Öpik 1924). For the inner orbits, we set the range to $1 < a_{\text{in}}/\text{AU} < 10^4$. The lower limit is motivated from the result of Section 2 that the number of potentially interesting systems drops rapidly as $a_{\text{in}} \lesssim 10 \text{ AU}$ due to general relativistic precession. This is also supported a posteriori from the simulations, given that we find few mergers with initial inner orbit semimajor axes less than a few AU. The upper limit is motivated by the fact that such very wide binaries quickly evaporate, and/or are dynamically unstable with respect to the MBH. The range of a_{out} is set to $0.01 < a_{\text{out}}/r_h < 2$. For smaller a_{out} , we find few mergers a posteriori, and our models do not apply for $a_{\text{out}} \gg r_h$.

We note that our distribution of the semimajor axis of the compact object binary differs from simulations of globular clusters, which typically predict distributions that are peaked around ~ 0.1 to $\sim 1 \text{ AU}$ (for binaries ejected from the cluster, e.g., Rodriguez et al. 2016). In the case of field binaries, the distribution is also biased towards small a_{in} , given that wider binaries are more susceptible to becoming unbound due to supernovae. This implies that the merger fractions would be lower if we had adopted such distributions for the initial semimajor axis of the compact object binary. This is borne out by a set of exploratory simulations that we carried out in which the inner binary was evolved from the MS until a compact object binary was formed using the BSE binary population synthesis code (Hurley et al. 2002), similar to the approach of Petrovich & Antonini (2017). In this exploratory set of simulations, the merger fractions were lower by a factor of ~ 10 , and this resulted in poor number statistics for the merging systems.

The inner and outer orbit eccentricities are sampled from a thermal distribution, $dN/de_i = 2e_i$ (with $0.01 < e_i < 0.95$). A thermal distribution is to be expected for the outer orbit due to dynamical interactions with the stellar cluster (Jeans

1919). Regarding the inner orbit, we expect that a significant eccentricity would typically be produced in the relatively wide ($a_{\text{in}} > 1$ AU) orbit due to the supernova kick associated with the formation of the second compact object. We note that there is little dependence of our results on the initial eccentricities.

Sampled systems that are dynamically unstable are rejected, where we use the stability criterion of [Mardling & Aarseth \(2001\)](#). In this approach, none of the systems are initially tidally disrupted by the MBH, i.e., in all cases $a_{\text{out}}(1 - e_{\text{out}}) > a_{\text{in}}[M_{\bullet}/(M_1 + M_2)]^{1/3}$. We compute the evaporation time-scale for the binary using equation (10), where we set $\sigma_{\star} = \sigma_{\star}(r_{\text{h}})$ if $r_{\text{out}} > r_{\text{h}}$ to take into account that the velocity dispersion outside of the radius of influence is typically constant.

The spins of the two compact objects are assumed to be initially coplanar with the inner orbit. This is likely not a good assumption if natal kicks were involved in the formation of the compact object binary. However, our aim is to show that LK-VRR coupling can very efficiently induce random spin-orbit orientations (see Section 5.2.3 below). Therefore, we choose to set up the system with zero initial spin-orbit alignments. Any randomization in the spin-orbit alignment can then clearly be attributed to the dynamical evolution. The spins are evolved according to the orbit-averaged PN geodesic equations of motion (e.g., [Schnittman 2004](#)), where we neglect the back-reaction of the spins on the orbit.

Each simulation is carried out twice: once with VRR included, and once without the effects of VRR. We consider two sets of simulations. In the ‘small’ set, we set the number of BH-BH binaries to be $N_{\text{MC}} = 10^3$, and consider 20 different combinations of M_{\bullet} and γ . The number of systems for each parameter combination in this set is relatively low, implying low merger number statistics. We also consider a ‘large’ set, in which we set $N_{\text{MC}} = 10^4$. In the large set, we consider the combination $M_{\bullet} = 10^4 M_{\odot}$ and $\gamma = 2$ (to maximize the absolute number of mergers), and the combination $M_{\bullet} = 4 \times 10^6 M_{\odot}$ and $\gamma = 1.3$, representative of the Galactic Center (GC; [Ghez et al. 2008](#); [Gillessen et al. 2009](#); [Fritz et al. 2016](#); [Schödel et al. 2018](#)).

5.1.2. Stopping conditions

The successfully-sampled systems are integrated for a duration of 10 Gyr or the evaporation time-scale (equation 10), whichever is shortest. In addition, we check for the following conditions during the simulations using root finding within the numerical integration of the ODEs (this ensures that no conditions are missed due to finite output times).

1. The time-scale for GW emission in the inner binary to shrink a_{in} by order itself, $t_{a,\text{GW}}$, is 10 times shorter than the time-scale for LK oscillations to reduce the inner binary periapsis distance $r_{\text{p,in}}$ by order itself, $t_{r_{\text{p}},\text{LK}}$.

Specifically, $10 t_{a,\text{GW}} < t_{r_{\text{p}},\text{LK}}$, where

$$\begin{aligned} t_{a,\text{GW}}^{-1} &\equiv \left| \frac{1}{a_{\text{in}}} \frac{da_{\text{in}}}{dt} \right|_{\text{GW}} \\ &= \frac{64 G^3 M_1 M_2 (M_1 + M_2)}{5 c^5 a_{\text{in}}^4 (1 - e_{\text{in}}^2)^{7/2}} \left(1 + \frac{73}{24} e_{\text{in}}^2 + \frac{37}{96} e_{\text{in}}^4 \right); \quad (25) \\ t_{r_{\text{p}},\text{LK}}^{-1} &\equiv \left| \frac{1}{r_{\text{p,in}}} \frac{dr_{\text{p,in}}}{dt} \right|_{\text{LK}} \\ &= \frac{75}{64} \sqrt{\frac{5}{3}} \frac{e_{\text{in}}}{\sqrt{1 - e_{\text{in}}^2}} \sqrt{\frac{G(M_1 + M_2)}{a_{\text{in}}^3}} \frac{M_{\bullet}}{M_1 + M_2} \left(\frac{a_{\text{in}}}{a_{\text{out}}} \right)^3 \\ &\quad \times (1 - e_{\text{out}}^2)^{-3/2}. \quad (26) \end{aligned}$$

Equation (25) follows directly from equation (5.6) of [Peters \(1964\)](#); to derive equation (26), we computed the rms average of the secular quadrupole-order LK equation for \dot{e}_{in} over all directions of $\hat{\mathbf{J}}_{\text{out}}$.

Once this condition is met, the binary is effectively decoupled from the MBH, and the evolution is dominated by the 2.5PN GW terms in the inner binary. We stop the subsequent integration, and flag the system as a compact object binary merger. The factor 10 in $10 t_{a,\text{GW}} < t_{r_{\text{p}},\text{LK}}$ is a ‘safety’ factor to ensure that the system is completely decoupled. We demonstrate that our criterion is robust by giving an example below in Section 5.2.1.

2. The secular approximation in the orbit-averaged three-body equations of motion breaks down (i.e., the semisecular or quasi-secular regime is reached). This can occur when the time-scale for the inner orbit angular-momentum to change by order itself becomes comparable to or even shorter than the inner or outer orbital periods, in which case averaging over the orbits is clearly no longer a good approximation. We assume that the semisecular regime is entered if ([Antonini et al. 2014](#))

$$\sqrt{1 - e_{\text{in}}} < 5\pi \frac{M_{\bullet}}{M_1 + M_2} \left[\frac{a_{\text{in}}}{a_{\text{out}}(1 - e_{\text{out}})} \right]^3. \quad (27)$$

In the semisecular regime, the system can remain dynamically stable, but the maximum eccentricities reached in the inner orbit can be potentially higher compared to the maximum eccentricities according to the doubly-averaged equations of motion ([Antonini & Perets 2012](#); [Antonini et al. 2014](#)). Here, we continue integrating the equations of motion using the secular equations, even after the semisecular regime is reached. We do record when the system enters the semisecular regime. This implies that our merger rates are likely underestimated. However, our focus is on the relative enhancement of the rates when VRR is taken into account. We do not expect that this approach introduces significant errors in the relative merger rates.

Also, we stop the integration if the system becomes dynamically unstable according to the criterion of [Mardling & Aarseth \(2001\)](#). Although we do check for this condition, it does not occur in the simulations since originally-unstable

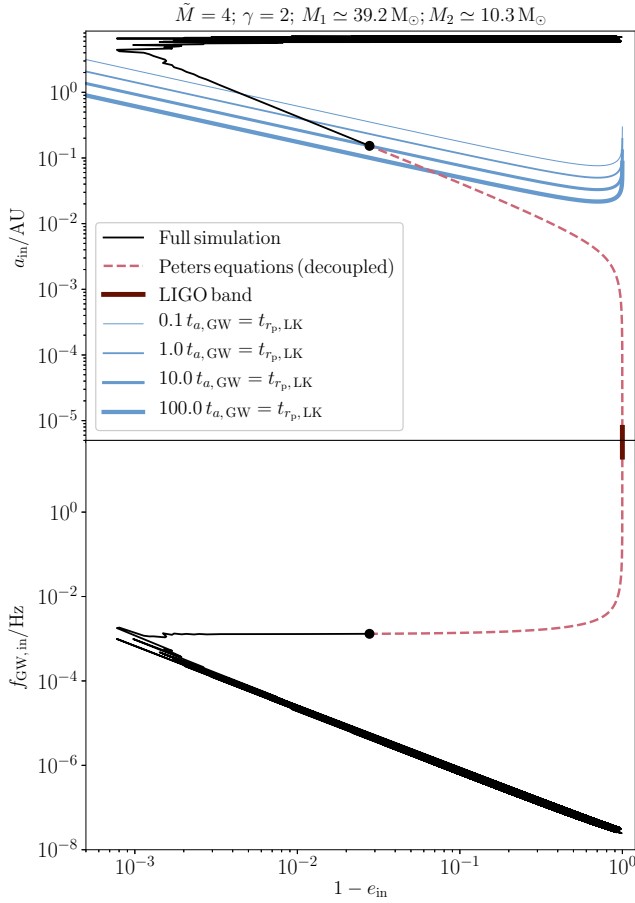


Figure 8. Example evolution of a system in which the inner binary merges due to coupled LK-VRR evolution. The top and bottom panels show evolutionary tracks in the $(1 - e_{\text{in}}, a_{\text{in}})$ and $(1 - e_{\text{in}}, f_{\text{GW,in}})$ planes, respectively, where $f_{\text{GW,in}}$ is the inner orbit GW frequency (see equation 28). Refer to the text for the initial conditions. Solid black lines: evolution according to the ‘full’ numerical simulations (including the three-body secular terms, terms associated with VRR, and PN terms); the black circles correspond to stopping condition (1) in Section 5.1.2. Red dashed lines: analytic solutions for 2.5PN evolution in isolated binaries according to Peters (1964). The thick red solid lines indicate the LIGO band ($f_{\text{GW,in}} > 20$ Hz). In the top panel, the blue solid curves show contours for which $t_{a,\text{GW}}$ (equation 25) and $t_{r_p,\text{LK}}$ (equation 26) are related by various factors, indicated in the legend.

systems were rejected, and a_{out} , e_{out} and the masses are assumed to be constant (also, note that a_{in} can only decrease due to the 2.5PN terms, bringing the system even further away from dynamical instability). Similarly, we check for tidal disruption of the binary by the MBH, i.e., $a_{\text{out}}(1 - e_{\text{out}}) < a_{\text{in}}[M_{\bullet}/(M_1 + M_2)]^{1/3}$, which does not occur in the simulations for similar reasons.

5.2. Results

5.2.1. Example

In Fig. 8, we give an example of the evolution in the $(1 - e_{\text{in}}, a_{\text{in}})$ plane (top panel), and the $(1 - e_{\text{in}}, f_{\text{GW,in}})$ plane

(bottom panel), of a system in which the inner binary eventually merges. Here, $f_{\text{GW,in}}$ is the peak GW frequency in the inner binary (i.e., the mode with the most power), calculated according to Wen (2003)

$$f_{\text{GW,in}} = \frac{1}{\pi} \sqrt{\frac{G(M_1 + M_2)}{a_{\text{in}}^3}} \frac{(1 + e_{\text{in}})^{1.1954}}{(1 - e_{\text{in}}^2)^{3/2}}. \quad (28)$$

The initial parameters in the example system are $M_{\bullet} = 10^4 M_{\odot}$, $\gamma = 2$, $M_1 \approx 39.2 M_{\odot}$, $M_2 \approx 10.3 M_{\odot}$, $a_{\text{in}} \approx 7.13$ AU, $a_{\text{out}} \approx 2.5 \times 10^3$ AU ≈ 0.012 pc, $e_{\text{in}} \approx 0.15$, $e_{\text{out}} \approx 0.43$, and $i_{\text{rel}} \approx 80^\circ$. The LK and VRR time-scales are comparable ($t_{\text{LK}} \approx 0.068$ Myr; $t_{\text{VRR}} \approx 0.11$ Myr, such that $\mathcal{R} \approx 0.63$); in the example, VRR is included, and high eccentricities are reached due to coupled LK-VRR evolution. Note that, although the initial relative inclination is relatively high, it is not high enough to trigger a merger in the absence of VRR.

As shown in Fig. 8, the inner binary semimajor axis decreases slightly due to the 2.5PN terms each time the eccentricity is high, resulting in a wide horizontal band in the $(1 - e_{\text{in}}, a_{\text{in}})$ plane. After ~ 680 Myr of evolution, the 2.5PN terms become more dominant and the binary starts to spiral in due to GW emission. The eccentricity oscillations then stop as a_{in} decreases, which can be ascribed to the increasing secular time-scale t_{LK} with decreasing a_{in} , whereas the 1PN precession time-scale decreases.

The end of the ‘full’ simulation, i.e., in which the three-body secular terms, terms associated with VRR, and PN terms are included, is marked with the black circles in Fig. 8. At this stage, the inner binary is clearly decoupled from perturbations of the MBH and the surrounding stellar cluster, and the evolution is dominated by the 2.5PN terms. The subsequent evolution is not computed in the ‘full’ simulation, but shown in Fig. 8 with the red dashed lines, which are based on the analytic solution of Peters (1964), i.e.,

$$a_{\text{in}}(e_{\text{in}}) = \frac{c_0 e_{\text{in}}^{12/19}}{1 - e_{\text{in}}^2} \left(1 + \frac{121}{304} e_{\text{in}}^2 \right)^{870/2299}, \quad (29)$$

where c_0 follows from the initial conditions (i.e., the black circles in Fig. 8). The parts of the curves corresponding to the LIGO band (i.e., a GW frequency higher than 20 Hz) are shown with thick solid dark red lines. The eccentricity when reaching the LIGO band, $e_{\text{in,LIGO}} \approx 2 \times 10^{-5}$, is small; this is generally the case in the Monte Carlo simulations (see Section 5.2.3 below).

In the top panel of Fig. 8, we also show with four solid blue lines several contours for which the GW and LK time-scales are related by factors ranging between 0.1 and 100 (refer to the legend). Since the ‘full’ simulations were stopped when $10 t_{a,\text{GW}} = t_{r_p,\text{LK}}$, the third contour intersects with the black circle. The contours show that there is not a strong sensitivity of the assumed factor between the time-scales, on whether or not the system would have been identified as a merger system. For example, if the criterion $t_{a,\text{GW}} = t_{r_p,\text{LK}}$ had been adopted, the ‘full’ simulation would have been stopped at a larger a_{in} , but still at a point in the $(1 - e_{\text{in}}, a_{\text{in}})$ -space in which the inner binary is decoupled.

5.2.2. Fractions

We distinguish between the following channels in the Monte Carlo simulations.

Fixed parameters	Fraction							
	No Interaction		No Interaction Semisecular		Merger		Merger Semisecular	
	VRR	No VRR	VRR	No VRR	VRR	No VRR	VRR	No VRR
$N_{MC} = 10^3$								
$\tilde{M}_\bullet = 4.0; \gamma = 1.3$	0.817 ± 0.029	0.976 ± 0.031	0.018 ± 0.004	0.006 ± 0.002	0.132 ± 0.011	0.013 ± 0.004	0.033 ± 0.006	0.005 ± 0.002
$\tilde{M}_\bullet = 4.0; \gamma = 2.0$	0.680 ± 0.026	0.965 ± 0.031	0.034 ± 0.006	0.012 ± 0.003	0.224 ± 0.015	0.019 ± 0.004	0.062 ± 0.008	0.004 ± 0.002
$\tilde{M}_\bullet = 4.3; \gamma = 1.3$	0.904 ± 0.030	0.986 ± 0.031	0.014 ± 0.004	0.004 ± 0.002	0.063 ± 0.008	0.007 ± 0.003	0.019 ± 0.004	0.003 ± 0.002
$\tilde{M}_\bullet = 4.3; \gamma = 2.0$	0.811 ± 0.029	0.974 ± 0.031	0.024 ± 0.005	0.015 ± 0.004	0.136 ± 0.012	0.009 ± 0.003	0.029 ± 0.005	0.002 ± 0.001
$\tilde{M}_\bullet = 4.7; \gamma = 1.3$	0.952 ± 0.031	0.988 ± 0.031	0.011 ± 0.003	0.004 ± 0.002	0.030 ± 0.005	0.006 ± 0.002	0.007 ± 0.003	0.002 ± 0.001
$\tilde{M}_\bullet = 4.7; \gamma = 2.0$	0.907 ± 0.030	0.988 ± 0.031	0.019 ± 0.004	0.007 ± 0.003	0.048 ± 0.007	0.004 ± 0.002	0.026 ± 0.005	0.001 ± 0.001
$\tilde{M}_\bullet = 5.0; \gamma = 1.3$	0.958 ± 0.031	0.988 ± 0.031	0.015 ± 0.004	0.008 ± 0.003	0.021 ± 0.005	0.004 ± 0.002	0.006 ± 0.002	0.000 ± 0.000
$\tilde{M}_\bullet = 5.0; \gamma = 2.0$	0.947 ± 0.031	0.990 ± 0.031	0.012 ± 0.003	0.007 ± 0.003	0.026 ± 0.005	0.002 ± 0.001	0.015 ± 0.004	0.001 ± 0.001
$\tilde{M}_\bullet = 5.3; \gamma = 1.3$	0.982 ± 0.031	0.996 ± 0.032	0.006 ± 0.002	0.002 ± 0.001	0.009 ± 0.003	0.002 ± 0.001	0.003 ± 0.002	0.000 ± 0.000
$\tilde{M}_\bullet = 5.3; \gamma = 2.0$	0.972 ± 0.031	0.994 ± 0.032	0.006 ± 0.002	0.002 ± 0.001	0.014 ± 0.004	0.002 ± 0.001	0.008 ± 0.003	0.002 ± 0.001
$\tilde{M}_\bullet = 5.7; \gamma = 1.3$	0.991 ± 0.031	0.997 ± 0.032	0.003 ± 0.002	0.001 ± 0.001	0.005 ± 0.002	0.002 ± 0.001	0.001 ± 0.001	0.000 ± 0.000
$\tilde{M}_\bullet = 5.7; \gamma = 2.0$	0.981 ± 0.031	0.993 ± 0.032	0.008 ± 0.003	0.003 ± 0.002	0.008 ± 0.003	0.002 ± 0.001	0.003 ± 0.002	0.002 ± 0.001
$\tilde{M}_\bullet = 6.0; \gamma = 1.3$	0.988 ± 0.031	0.994 ± 0.032	0.005 ± 0.002	0.002 ± 0.001	0.007 ± 0.003	0.004 ± 0.002	0.000 ± 0.000	0.000 ± 0.000
$\tilde{M}_\bullet = 6.0; \gamma = 2.0$	0.985 ± 0.031	0.997 ± 0.032	0.001 ± 0.001	0.000 ± 0.000	0.011 ± 0.003	0.003 ± 0.002	0.003 ± 0.002	0.000 ± 0.000
$\tilde{M}_\bullet = 6.3; \gamma = 1.3$	0.989 ± 0.031	0.994 ± 0.032	0.002 ± 0.001	0.001 ± 0.001	0.008 ± 0.003	0.005 ± 0.002	0.001 ± 0.001	0.000 ± 0.000
$\tilde{M}_\bullet = 6.3; \gamma = 2.0$	0.988 ± 0.031	0.995 ± 0.032	0.002 ± 0.001	0.002 ± 0.001	0.007 ± 0.003	0.001 ± 0.001	0.003 ± 0.002	0.002 ± 0.001
$\tilde{M}_\bullet = 6.7; \gamma = 1.3$	0.994 ± 0.032	0.997 ± 0.032	0.001 ± 0.001	0.000 ± 0.000	0.005 ± 0.002	0.003 ± 0.002	0.000 ± 0.000	0.000 ± 0.000
$\tilde{M}_\bullet = 6.7; \gamma = 2.0$	0.993 ± 0.032	0.995 ± 0.032	0.002 ± 0.001	0.002 ± 0.001	0.003 ± 0.002	0.002 ± 0.001	0.002 ± 0.001	0.001 ± 0.001
$\tilde{M}_\bullet = 7.0; \gamma = 1.3$	0.995 ± 0.032	0.996 ± 0.032	0.001 ± 0.001	0.000 ± 0.000	0.004 ± 0.002	0.004 ± 0.002	0.000 ± 0.000	0.000 ± 0.000
$\tilde{M}_\bullet = 7.0; \gamma = 2.0$	0.993 ± 0.032	0.997 ± 0.032	0.001 ± 0.001	0.001 ± 0.001	0.003 ± 0.002	0.002 ± 0.001	0.002 ± 0.001	0.000 ± 0.000
$N_{MC} = 10^4$								
$\tilde{M}_\bullet = 4.0; \gamma = 2.0$	0.683 ± 0.008	0.966 ± 0.010	0.032 ± 0.002	0.010 ± 0.001	0.227 ± 0.005	0.021 ± 0.001	0.059 ± 0.002	0.003 ± 0.001
$\tilde{M}_\bullet = 6.6; \gamma = 1.3$	0.989 ± 0.010	0.994 ± 0.010	0.002 ± 0.000	0.001 ± 0.000	0.007 ± 0.001	0.004 ± 0.001	0.001 ± 0.000	0.001 ± 0.000

Table 2

Fractions of outcomes from the Monte Carlo calculations. The fractions are based on N_{MC} simulations for each parameter combination, with and without the inclusion of VRR. Each row corresponds to a different combination of $\tilde{M}_\bullet \equiv \log_{10}(M_\bullet/M_\odot)$ and γ , indicated in the first column. We show results for the small set of simulations ($N_{MC} = 10^3$; top part of the table), and the large set ($N_{MC} = 10^4$; bottom part of the table). Fractions are rounded to three digits, and Poisson errors are given for each entry.

1. The binary does not merge, and the binary+MBH system remains outside of the semisecular regime at all times (‘no interaction’).
2. The binary does not merge, but the binary+MBH system does enter the semisecular regime at any time during the evolution (‘no interaction; semisecular’).
3. Due to high eccentricities in the inner orbit, stopping condition (1) (see Section 5.1.2) is met without entering the semisecular regime. The binary will merge due to orbital energy loss due to GW emission (‘merger’).
4. Similar to case (3), but here, during any point of the evolution the semisecular regime was also entered (‘merger; semisecular’).

In Table 2, we show the fractions of these channels in the simulations for the ‘small’ set of simulations ($N_{MC} = 10^3$; top part of the table), and the ‘large’ set of simulations ($N_{MC} = 10^4$; bottom part of the table). The fractions are given for simulations with VRR included (‘VRR’), and excluded (‘No VRR’). Each row corresponds to a different combination of $\tilde{M}_\bullet \equiv \log_{10}(M_\bullet/M_\odot)$ and γ , indicated in the first column. Poisson errors are given for each entry. As to be expected, the merger fractions for $M_\bullet = 10^4 M_\odot$ and $\gamma = 2$ are consistent within the error bars between the ‘small’ and ‘large’ sets.

A dynamical instability of the binary+MBH system does not occur in the simulations; therefore, the corresponding fractions are not given in Table 2. This can be attributed to the constancy of e_{out} in the simulations (note that the other

quantities occurring in the stability criterion of [Mardling & Aarseth \(2001\)](#) are also constant in our simulations).

We note the following trends in the fractions shown in Table 2.

- The merger fractions with VRR included are the largest for $M_\bullet = 10^4 M_\odot$ and $\gamma = 2$, in which case $f_{merge} \approx 0.2$. For smaller M_\bullet and γ , the merger fractions are smaller. For $M_\bullet = 10^7 M_\odot$, the fractions are close to zero.
- Typically, the merger fractions are enhanced by VRR by a factor of up to ~ 10 .
- Depending on M_\bullet and γ , for $\sim 10\%$ to $\sim 50\%$ of the mergers the semisecular regime is entered (i.e., before reaching stopping condition 1 in Section 5.1.2).
- Of the non-interacting systems, up to a few per cent enter the semisecular regime. The fraction of these systems is a few times larger if VRR is included.

5.2.3. Orbital distributions

In this section, we focus on the properties of the systems that undergo the outcomes described in Section 5.2.2, specializing to the ‘large’ set of simulations ($N_{MC} = 10^4$) with $M_\bullet = 10^4 M_\odot$ and $\gamma = 2$. The results are qualitatively similar for the large GC-like set ($M_\bullet = 4 \times 10^6 M_\odot$ and $\gamma = 1.3$); however, the statistics in the former simulations are much better because of the larger merger fractions (see Table 2). Therefore, we focus on the case $M_\bullet = 10^4 M_\odot$ and $\gamma = 2$.

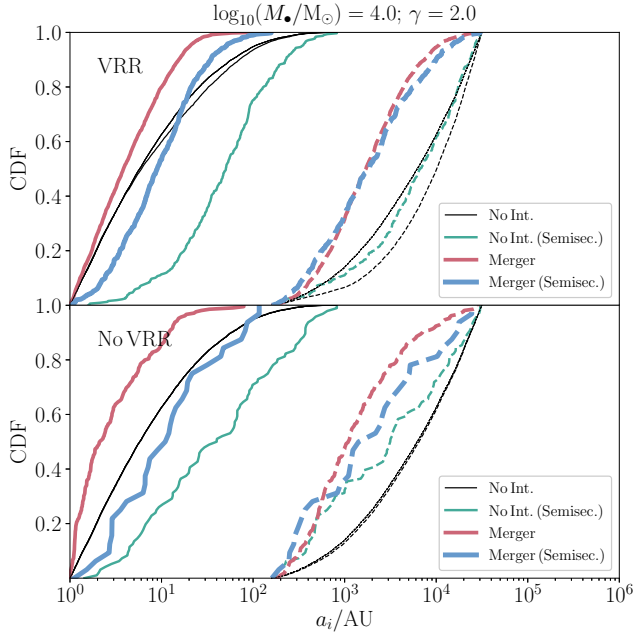


Figure 9. Cumulative distributions of the inner (solid lines) and outer (dashed lines) orbit semimajor axes for the ‘large’ simulations ($N_{\text{MC}} = 10^4$), for which $M_{\bullet} = 10^4 M_{\odot}$, and $\gamma = 2$. The top (bottom) panels apply to the simulations with (without) VRR. The cases shown are no interaction (black lines), no interaction but entering the semisecular regime at any point in the evolution (green lines), merger (red lines), and merger while also entering the semisecular regime (blue lines). The thin black solid (dashed) lines show the initial distributions of the inner (outer) semimajor axes for *all* systems (i.e., not making a distinction to the outcome).

Semimajor axes — In Fig. 9, we show the distributions of the inner (solid lines) and outer (dashed lines) orbit semimajor axes. In this and in following figures, the top (bottom) panels apply to the simulations with (without) VRR. The cases shown are no interaction (black lines), no interaction but entering the semisecular regime at any point in the evolution (green lines), merger (red lines), and merger while also entering the semisecular regime (blue lines). The thin black solid (dashed) lines show the initial distributions of the inner (outer) semimajor axes for *all* systems (i.e., not making a distinction with respect to the outcome).

The typical initial inner orbit semimajor axis for the merging systems is ~ 10 AU. There are few mergers with small a_{in} , which can be attributed to relativistic precession, as noted before in Section 2.7. Merger systems that also enter the semisecular regime typically have larger a_{in} , which can be understood from equation (27): more compact systems are more susceptible to entering the semisecular regime. A similar property applies to the non-interacting semisecular systems. Overall, the semimajor axis distributions do not vary greatly between the ‘VRR’ and ‘No VRR’ cases.

Complementary to Fig. 9, we show in Fig. 10 the merger fractions (including both the semisecular and non-semisecular mergers) as a function of the outer orbit semimajor axis, a_{out} , for the VRR (solid line) and no VRR (dashed line) cases. With VRR included, the merger fraction peaks around 10^3 AU, which corresponds to $\sim 0.1 r_{\text{h}}$ for the simulation with $M_{\bullet} = 10^4 M_{\odot}$ and $\gamma = 2$. This is consistent with Fig. 1, in

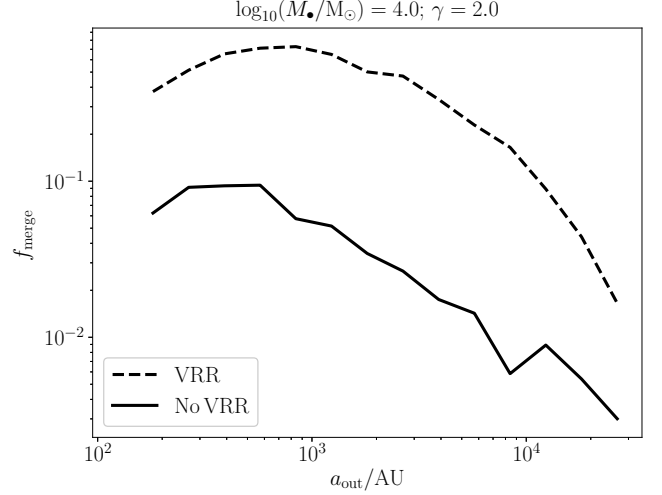


Figure 10. Merger fractions (including both the semisecular and non-semisecular mergers) as a function of the outer orbit semimajor axis, a_{out} , for the VRR (solid line) and no VRR (dashed line) cases.

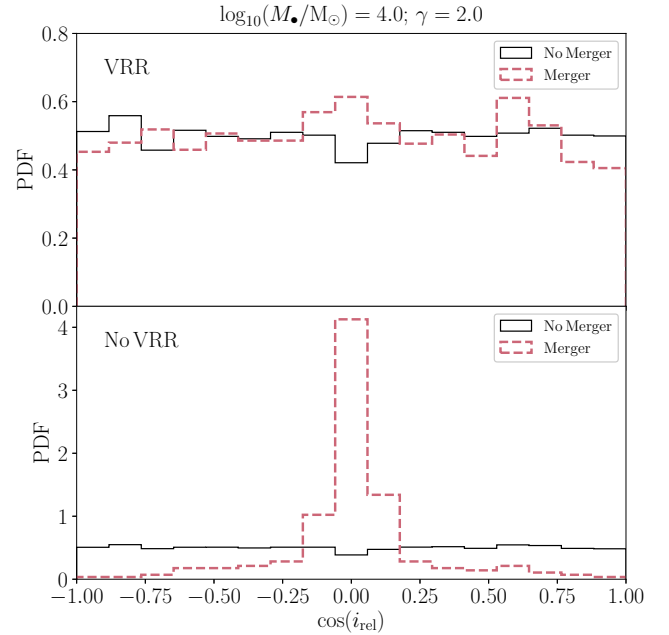


Figure 11. Distributions from the Monte Carlo simulations of the initial mutual inclinations between the inner and outer orbits, arranged by merger outcomes (red dashed lines), and non-merger outcomes (black solid lines). Top (bottom) panels apply to simulations with (without) VRR. The initial distribution of $\cos(i_{\text{rel}})$ was assumed to be flat between -1 and 1.

the sense that the latter figure shows that for comparable parameters, the regions of interest lie around $r = 0.1 r_{\text{h}}$. The enhancement relative to the case without VRR is ~ 10 , and is not strongly dependent on a_{out} .

Inclinations — The distributions of the initial mutual inclinations between the inner and outer orbits are shown in Fig. 11. Here, we show distributions for the merging systems (red dashed lines), and the non-merging systems (black solid

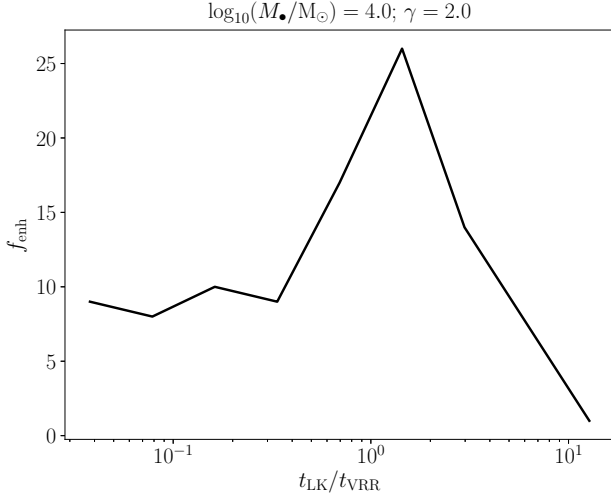


Figure 12. The enhancement factor due to VRR of the mergers in the Monte Carlo simulations, i.e., the number of mergers in the case of VRR divided by the number of mergers without VRR, binned in terms of the adiabatic parameter $\mathcal{R} \equiv t_{\text{LK}}/t_{\text{VRR}}$ (see equation 12).

lines), combining results from the systems that enter and that do not enter the semisecular regime. Initially, random orbital orientations were assumed (uniform distribution in $\cos i_{\text{rel},0}$). Without VRR, the inclination distributions of the semisecular and merger systems are highly peaked around 90° . This can be easily understood by noting that these cases are associated with very high eccentricities (see also Fig. 13); therefore, the initial inclination should be close to 90° (see equation 22). With VRR included, the distributions for the same channels are not peaked, and broadly distributed along all inclinations. This can be understood by noting that VRR can induce high mutual inclinations, which can subsequently lead to high inner orbit eccentricities through LK evolution. Therefore, no high initial mutual inclination is required, and this is the key ingredient to the enhanced merger rates when VRR is taken into account.

Adiabatic parameter — In Fig. 12, we show the enhancement factor due to VRR of the mergers in the Monte Carlo simulations, i.e., the number of mergers in the case of VRR divided by the number of mergers without VRR, binned in terms of the adiabatic parameter $\mathcal{R} \equiv t_{\text{LK}}/t_{\text{VRR}}$ (see equation 12). We only include bins in \mathcal{R} with more than two mergers in the case without VRR. The enhancement factor is peaked near $\mathcal{R} = 1$, which is in agreement with the scale-free results of Section 4. Some enhancement is already present at $\mathcal{R} \sim 0.1$, which is consistent with Fig. 7 in the sense that in the latter figure, the cumulative distribution of the maximum eccentricity is already significantly enhanced from the case without VRR ($\mathcal{R} = 0$) for $\mathcal{R} \sim 0.1$.

Eccentricity at the LIGO band — In Fig. 13, we show the distributions of the eccentricity of the merging binaries when they enter the LIGO band, $e_{\text{in,LIGO}}$. Here, we compute $e_{\text{in,LIGO}}$ by assuming that $e_{\text{in,LIGO}}$ is small, such that (using equations 28 and 29)

$$e_{\text{in,LIGO}} \approx \left[\frac{1}{\pi f_{\text{GW,LIGO}}} \sqrt{\frac{G(M_1 + M_2)}{c_0^3}} \right]^{19/18}, \quad (30)$$

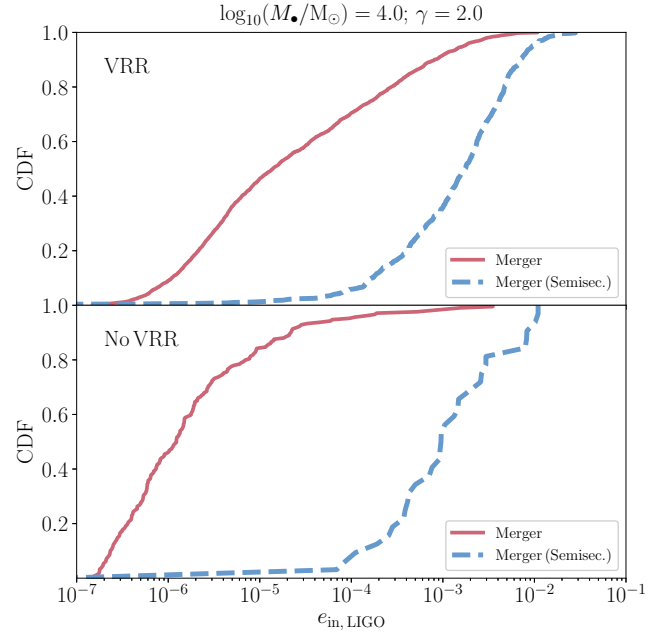


Figure 13. Cumulative distributions of the eccentricity of the merging inner binaries when they enter the LIGO band, computed using equation (30). Blue (red) lines show systems that do (not) enter the semisecular regime.

where $f_{\text{GW,LIGO}} = 20 \text{ Hz}$, and c_0 is determined using equation (29) and the simulation data at the moment of the merger stopping condition (as shown above, at this point the inner binary is decoupled). Equation (30) applies only if $e_{\text{in,LIGO}}$ is small; we find a posteriori that this is indeed the case — the true GW frequency at $e_{\text{in,LIGO}}$ in our simulations deviates from $f_{\text{GW,LIGO}}$ by no more than a few per cent.

The typical eccentricity when entering the LIGO band is small. The median value in the VRR case is $\sim 10^{-5}$, with maximum values of $\sim 10^{-2}$ for the systems that also entered the semisecular regime (blue lines in Fig. 13). The latter case is associated with very high eccentricities, explaining the typically larger values of $e_{\text{in,LIGO}}$. The values of $e_{\text{in,LIGO}}$ are typically larger if VRR is included. This can be explained by noting that the typical excited eccentricities in the VRR case are larger compared to the ‘pure’ LK case.

Masses — In Fig. 14, we show the distributions of the Chirp mass, $\mathcal{M} = (M_1 M_2)^{3/5} / (M_1 + M_2)^{1/5}$, for the merging systems in the simulations. The initial distributions for all systems are shown with the thin black solid lines. The merger systems have slightly higher Chirp masses compared to all systems, although the differences are small — it is unlikely that these differences have observational implications.

We show a similar figure for the mass ratios $q \equiv M_2/M_1$ in Fig. 15. The mergers show no discernible dependence on q .

Spins — Finally, we show in Fig. 16 the distributions of the projected spin parameter, i.e.,

$$\chi_{\text{eff}} = \frac{M_1 \chi_1 \cos(\theta_1) + M_2 \chi_2 \cos(\theta_2)}{M_1 + M_2}, \quad (31)$$

where χ_i is the normalized spin parameter of star i , and θ_i is the angle between the spin vector of star i and the inner

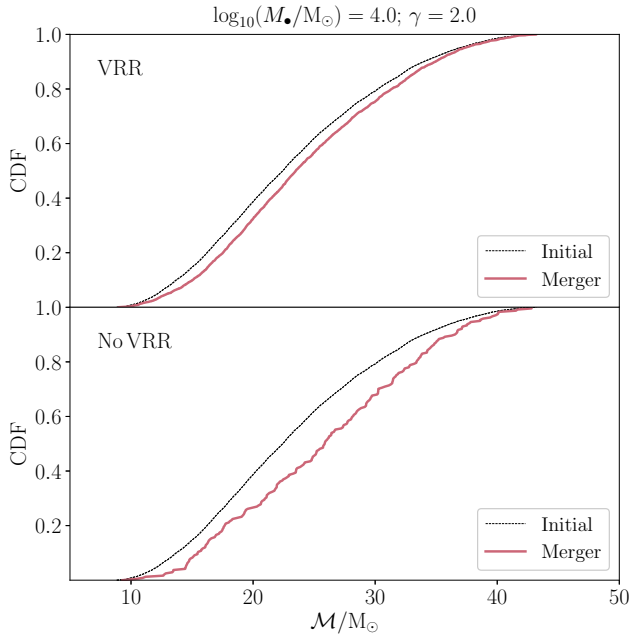


Figure 14. Cumulative distributions of the Chirp masses, $\mathcal{M} = (M_1 M_2)^{3/5} / (M_1 + M_2)^{1/5}$, for the mergers in the Monte Carlo simulations (solid red lines). The thin black dotted lines show the initial distributions. Top (bottom): with (without) VRR.

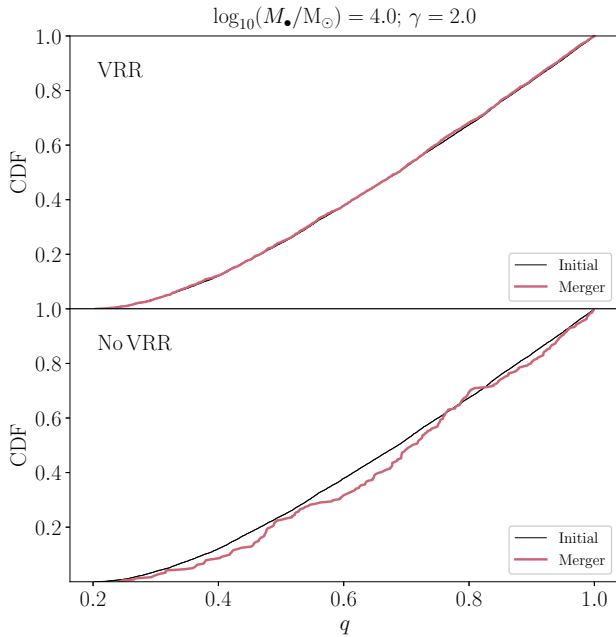


Figure 15. Cumulative distributions of the binary mass ratio, $q \equiv M_2/M_1$, for the mergers in the Monte Carlo simulations (solid red lines). The thin black dotted lines show the initial distributions. Top (bottom): with (without) VRR.

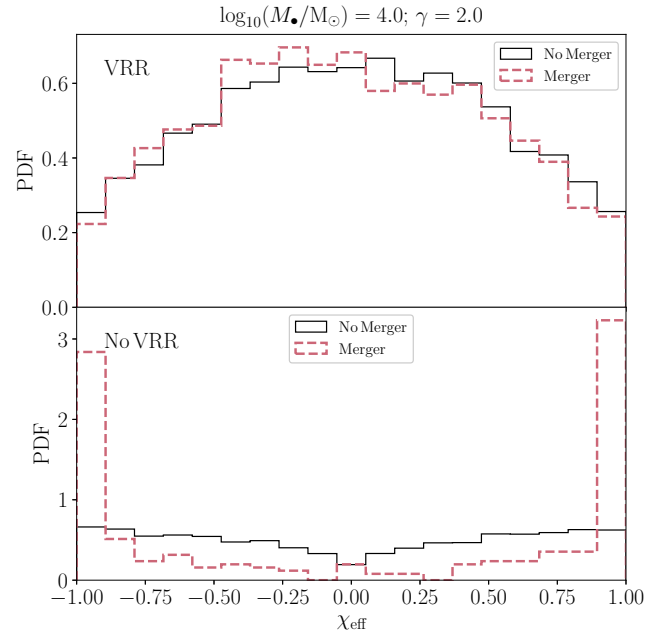


Figure 16. Distributions of the final χ_{eff} (see equation 31) for the four outcomes in the Monte Carlo simulations.

orbit angular-momentum vector. For simplicity, we assume that the two compact objects are maximally spinning, i.e., $\chi_1 = \chi_2 = 1$. The distributions of χ_{eff} are shown at the end of the simulations for merging and non-merging systems (both including the semiseccular systems). Note that for the merger systems, this corresponds to a point in the evolution in which the inner binary is decoupled from the MBH and the stellar cluster. Near the LIGO band, the higher-order spin-spin and spin-orbit terms will become important and change the individual spin orbit angles. However, χ_{eff} does not change during this process at the 2.5PN level. The initial spin-orbit angles were assumed to be zero. We note that the spin dynamics of compact objects in triple systems (without taking into account the effects of VRR) have been considered by a number of authors (Liu & Lai 2017; Antonini et al. 2017a; Liu & Lai 2018).

Without VRR, the distribution of χ_{eff} for the merging systems is peaked near -1 and $+1$. With VRR included, the distributions of χ_{eff} are broadly distributed between -1 and $+1$, with a peak around 0 , indicative of random spin-orbit alignment. This can be ascribed to the coupling of LK oscillations with VRR: VRR continuously adjusts the outer orbital angular momentum vector independent of the initial mutual inclination i_{rel} , and these changes are transmitted to the inner orbit through the LK mechanism, producing spin-orbit misalignment for both merging and non-merging systems. Given that the initial spin-orbit alignment was assumed to be zero, the top panel of Fig. 16 shows that LK-VRR is very effective at producing random spin-orbit orientations.

5.2.4. Stopping times

In Fig. 17, we show the distributions of the stopping times arranged by the outcomes. For the non-merging systems, the stopping times are either set by the evaporation time-scale or 10 Gyr; for the mergers, the stopping time is the time when GW emission started to dominate over the LK dynamics; the

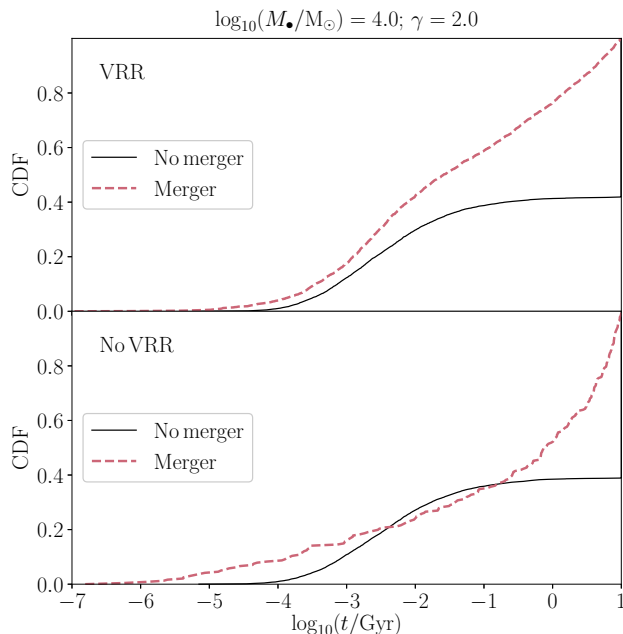


Figure 17. Cumulative distributions of the stopping times in the Monte Carlo simulations arranged by the outcomes (merger: red dashed lines; no merger: solid black lines).

true merging time is very close to this (see Section 5.1.2). The merger times in the simulations span a wide range between ~ 0.1 Myr, and 10 Gyr. With VRR included, the median stopping time is ~ 100 Myr. The late mergers are associated with a slower type of evolution in which the semimajor axis decreases only slightly at high eccentricities, until finally the 2.5PN terms start to dominate and the inner binary becomes decoupled.

Some, but not all mergers are limited by binary evaporation. This is illustrated in Fig. 18, in which the distributions are shown of the evaporation time-scale arranged by the outcomes. About 60% of the mergers with VRR included have evaporation time-scales longer than 10 Gyr.

5.2.5. Delay-time distributions

From the simulations, we determine the delay-time distributions (DTDs), i.e., the number of events per unit time. We consider the mergers in the ‘large’ set of simulations with $M_{\bullet} = 10^4 M_{\odot}$ and $\gamma = 2$, and include the mergers in which the semiseccular regime was entered. The resulting DTDs are shown in the top panel of Fig. 19. Dashed (solid) lines apply to the simulations with (without) VRR. For both cases with and without VRR, the DTDs are approximately inversely proportional with time. However, the absolute normalization of the DTDs is significantly higher with VRR included; the bottom panel in Fig. 19 shows the enhancement factor of the DTDs of the cases with VRR relative to no VRR. The enhancement factor is a function of time; it peaks at ~ 60 around 4 Myr, and drops toward ≈ 5 at 10^4 Myr.

6. DISCUSSION

6.1. Uncertainties in the integrations

As mentioned in Section 2, galactic nuclei are complex dynamical environments. Our Monte Carlo simulations (Section 5), although the first to include the effects of VRR in the

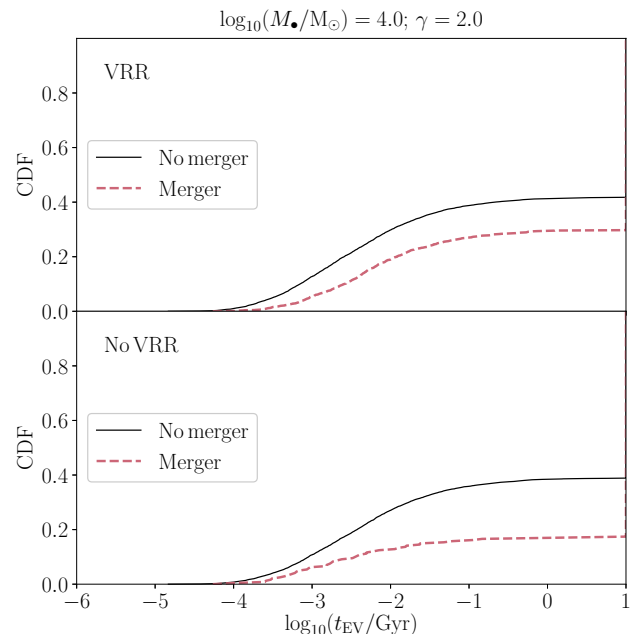


Figure 18. Cumulative distributions of the evaporation times (see equation 10) in the Monte Carlo simulations arranged by the outcomes (merger: red dashed lines; no merger: solid black lines).

context of the secular (orbit-averaged) LK problem, did not include all effects. Here, we comment on some of the processes that we did not consider, and should be included in future work.

As mentioned in Section 1, the torques exerted by the stellar cluster not only affect the orientation of an orbit around an MBH, but also the magnitude of its angular momentum. This process, known as SRR, was not included in the simulations. We argued in Section 2 that the SRR time-scale is typically longer than the VRR time-scale. However, the merging of the inner binary can occur after many LK cycles, corresponding typically to times $\gg t_{\text{VRR}}$ (since typically $\mathcal{R} \sim 1$ to reach high eccentricities, which are necessary for merging systems), and SRR can affect the outer orbit eccentricity on these longer time-scales. This could be important, since e_{out} changes both the efficiency of VRR and the LK process. More dramatically, an increased e_{out} could bring the binary sufficiently close to the MBH for the former to be tidally disrupted (Hills 1988).

Other effects that were neglected in the simulations are changes of the outer orbital parameters due to NRR and due to dynamical friction (DF). NRR in particular could be important if the mass function of the stellar background is top heavy, significantly reducing the NRR time-scale (see equation 9); this is an effect that we have ignored. DF could be important if the binary is much more massive than the typical background star, which is the case in our simulations (on average, $M_{\text{bin}} \equiv M_1 + M_2 = 60 M_{\odot}$, such that $M_{\text{bin}}/m_{\star} = 60$). The DF time-scale can be estimated as $t_{\text{DF}} \sim t_{\text{NR}} (m_{\star}/M_{\text{bin}}) \sim t_{\text{NR}}/60$ (Spitzer 1987; Alexander & Hopman 2009), implying that DF could be important in our simulations.

NRR and DF can affect the binary in several ways. First, a change in the outer binary semimajor axis and eccentricity can bring the binary into a different dynamical regime, since \mathcal{R} (see equation 12) is a function of both a_{out} and e_{out} . Also, the binary can migrate to regions with shorter evaporation time-

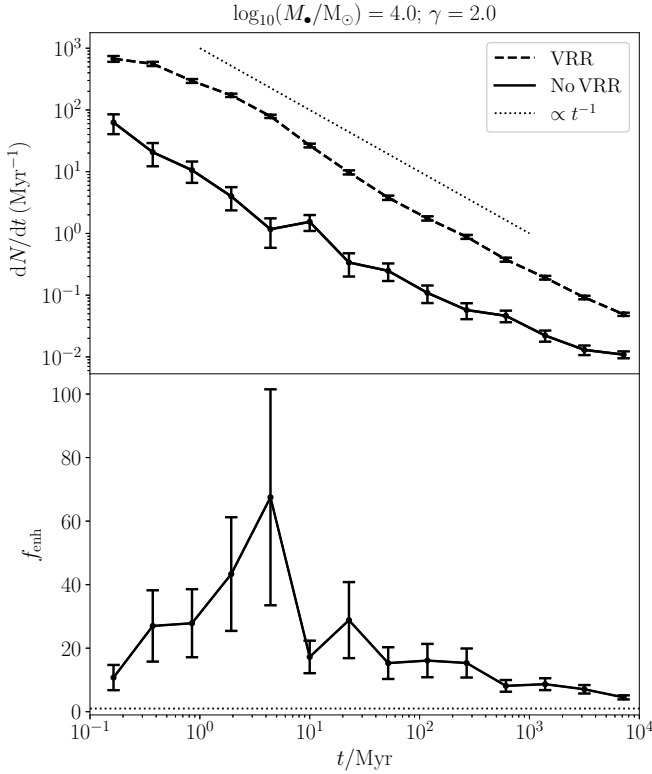


Figure 19. Top panel: DTDs of the mergers in the ‘large’ Monte Carlo simulation set with $M_{\bullet} = 10^4 M_{\odot}$ and $\gamma = 2$. Dashed (solid) lines apply to the simulations with (without) VRR. Error bars are based on Poisson statistics. The black dotted line shows a $\propto t^{-1}$ -dependence. Bottom panel: the enhancement factor, i.e., the ratio of the DTDs for the cases with and without VRR, as a function of time. The horizontal black dashed line shows an enhancement factor of 1. scales, such that the binary may not survive until a merger is triggered. Alternatively, the binary can be brought too close to the MBH and be tidally disrupted.

6.2. Estimates of absolute merger rates

Although the focus of this paper is on the *relative enhancement* of VRR on the rates of LK-induced mergers of binaries in galactic nuclei, we here estimate the absolute BH-BH binary merger rates based on our Monte Carlo simulations. A large number of assumptions must be made in order to make these estimates, and we emphasize that the numbers given here are extremely uncertain. The uncertainties in the absolute rates can be considered to be at least one order of magnitude, and up to several orders of magnitude.

6.2.1. GC

First, we consider our fiducial GC model ($M_{\bullet} = 4 \times 10^6 M_{\odot}$; $\gamma = 1.3$). We follow similar assumptions as Petrovich & Antonini (2017). Let n_{gal} be the number density of Milky-Way-like galaxies, Γ_{CO} be the formation rate of compact objects (number per unit time), f_{CO} the fraction of stars that evolve to compact object binaries (this includes the binary fraction), f_{merge} the merger fractions in the Monte Carlo simulations (Section 5), and f_{calc} the fraction of calculated systems relative to the underlying binary population. The merger rate

(number per unit time per unit volume) is then estimated by

$$\Gamma \sim n_{\text{gal}} \Gamma_{\text{CO}} f_{\text{CO}} f_{\text{merge}} f_{\text{calc}}. \quad (32)$$

We adopt a number density of galaxies of $n_{\text{gal}} \approx 0.02 \text{ Mpc}^{-3}$ (Conselice et al. 2005; Kopparapu et al. 2008).

We use simple arguments to estimate the compact object formation rate (for more detailed studies, see, e.g., Aharon & Perets 2015; Aharon et al. 2016). Assuming constant star formation, Löckmann et al. (2010) find that $\sim 10^4$ ($\sim 10^5$) BHs are formed for $10^6 M_{\odot}$ of mass in stars and stellar remnants, assuming a canonical (top-heavy) initial-mass function (IMF). Scaling these numbers to the GC, for which the total mass of stars formed in ~ 10 Gyr is $\sim 10^7 M_{\odot}$ (Schödel et al. 2014; Feldmeier-Krause et al. 2017; Schödel et al. 2018), this implies that the rate of compact object formation in the GC is $\Gamma_{\text{CO}} \sim 10^{-5} \text{ yr}^{-1}$ ($\Gamma_{\text{CO}} \sim 10^{-4} \text{ yr}^{-1}$) assuming a canonical (top-heavy) IMF.

Based on the BSE binary population synthesis code (Hurley et al. 2002), Petrovich & Antonini (2017) find that the fraction of stars forming compact object binaries is 0.025 (0.045) for a canonical (top-heavy) IMF. Here, the canonical (top-heavy) IMF is defined as $dN/dm \propto m^{-2.3}$ ($dN/dm \propto m^{-1.7}$). In these fractions, which are related to f_{CO} , Petrovich & Antonini (2017) implicitly assumed a MS binary fraction of unity. The underlying distributions of the binary properties in our simulations are different from those of Petrovich & Antonini (2017), implying that the appropriate values of f_{CO} are not necessarily the same as in Petrovich & Antonini (2017). Nevertheless, we let f_{CO} be motivated by the results of Petrovich & Antonini (2017), and so we set $f_{\text{CO}} = 0.25$ ($f_{\text{CO}} = 0.05$) for the canonical (top-heavy) IMF.

From Table 2, we adopt a merger fraction of $f_{\text{merge}} = 0.008$ and $f_{\text{merge}} = 0.005$ for the cases with and without VRR, respectively (we combine the merger fractions in the semisecular and non-semisecular regimes). We note that these merger fractions are based on simulations in which we assumed a Salpeter mass function for the stellar cluster (i.e., $m_{\star} \equiv \langle m^2 \rangle^{1/2} = 1 M_{\odot}$, see Section 2). With a top-heavy mass function, the merger fractions could be different since m_{\star} affects the VRR and evaporation time-scales. Here, we neglect this complication, and assume that f_{merge} is the same for the standard and top-heavy mass functions.

We estimate the calculated fraction, f_{calc} , by computing the fraction of orbits in our Monte Carlo simulations relative to the entire population, assuming that the semimajor axis distribution of the latter ranges between $\sim 10^{-2}$ and $\sim 10^6$ AU. For the GC model, the simulated binaries have semimajor axes ranging between ~ 1 and $\sim 10^3$ AU. Given that the distribution in a_{in} is assumed to be flat in $\ln(a_{\text{in}})$, this implies that $f_{\text{calc}} \sim \ln(10^3)/\ln(10^6) = 1/2$.

With the above assumptions, we find merger rates of $\Gamma_{\text{VRR}} = 0.02 \text{ Gpc}^{-1} \text{ yr}^{-1}$ ($\Gamma_{\text{VRR}} = 0.4 \text{ Gpc}^{-1} \text{ yr}^{-1}$) assuming a canonical (top-heavy) IMF if VRR is included. Without VRR, we find $\Gamma_{\text{No VRR}} \approx 0.013 \text{ Gpc}^{-1} \text{ yr}^{-1}$ ($\Gamma_{\text{No VRR}} = 0.25 \text{ Gpc}^{-1} \text{ yr}^{-1}$) assuming a canonical (top-heavy) IMF.

For reference, predictions of the BH merger rate for globular clusters include 2–20 $\text{Gpc}^{-3} \text{ yr}^{-1}$ (Rodríguez et al. 2016), $> 6.5 \text{ Gpc}^{-3} \text{ yr}^{-1}$ (Park et al. 2017), $> 5.4 \text{ Gpc}^{-3} \text{ yr}^{-1}$ (Askar et al. 2017), and 15–100 $\text{Gpc}^{-3} \text{ yr}^{-1}$ (Fragione & Kocsis 2018). For nuclear star clusters without MBHs, the rates have been predicted to be $\sim 1 \text{ Gpc}^{-3} \text{ yr}^{-1}$ (Antonini & Rasio 2016). The BH-BH merger rate inferred by LIGO is 12–213 $\text{Gpc}^{-1} \text{ yr}^{-1}$ (Abbott et al. 2017a).

Our numbers can be considered to be low compared to the above numbers. This indicates that VRR cannot sufficiently increase the merger rates of BH-BH binaries enough to make a significant contribution to the LIGO rate. However, the enhancement of f_{merge} due to VRR is small for GC-like galactic nuclei (i.e., a factor of $0.008/0.005 = 1.6$). We have shown that the enhancement of f_{merge} is much more significant for galactic nuclei with lower MBH masses (up to ~ 10 for $M_{\bullet} = 10^4 M_{\odot}$ and $\gamma = 2$).

6.2.2. Other galactic nuclei

Here, we make crude estimates for the merger rates in other galactic nuclei based on our ‘small’ set of simulations ($N_{\text{MC}} = 10^3$). The largest merger fractions in the simulations occur for low MBH masses of $10^4 M_{\odot}$; the existence of galactic nuclei with MBHs with such low masses is highly uncertain. Here, we assume that galactic nuclei with MBHs of such low mass exist, and estimate their number density as follows.

The luminosity function (number density per unit luminosity) for galaxies with MBH masses $\lesssim 10^8 M_{\odot}$ is approximately $\phi(L) \propto L^{-1}$ (Aller & Richstone 2002). Since the Faber-Jackson relation, approximately $L \propto \sigma_{\star}^4$ (Faber & Jackson 1976), and the $M_{\bullet} - \sigma_{\star}$ relation, approximately $M_{\bullet} \propto \sigma_{\star}^4$ (Merritt & Ferrarese 2001), have approximately the same scaling with σ_{\star} , we assume that $L \propto M_{\bullet}$. This implies that the number density of MBHs per unit mass scales as $\phi(M_{\bullet}) \propto M_{\bullet}^{-1}$ (Aller & Richstone 2002; we also assume an MBH occupation fraction of unity). This implies that the M_{\bullet} -integrated number density is

$$n_{\text{gal}} \propto \int \phi(M_{\bullet}) dM_{\bullet} \propto \log(M_{\bullet}), \quad (33)$$

i.e., the dependence of n_{gal} on M_{\bullet} is weak (logarithmic). Therefore, for simplicity, we assume that n_{gal} is completely independent of M_{\bullet} , and set $n_{\text{gal}} = 0.02 \text{ Mpc}^{-3}$ (Conselice et al. 2005; Kopparapu et al. 2008), as for the GC case in Section 6.2.1.

The compact object formation rate, Γ_{CO} , is also highly uncertain. We make two limiting assumptions. (1) Γ_{CO} is weakly dependent of M_{\bullet} , which would be appropriate if the compact objects are supplied to the galactic nucleus by NRR. In particular, assuming the $M_{\bullet} - \sigma$ relation in the form $M_{\bullet} \propto \sigma^{\beta}$, one can show that (e.g., Alexander & Bar-Or 2017)

$$\Gamma_{\text{CO}} = \frac{\gamma_{\text{CO}} N_{\star}(r_{\text{h}})}{t_{\text{NRR}}(r_{\text{h}})} \propto M_{\bullet}^{\frac{3-\beta}{\beta}}. \quad (34)$$

The latter is weakly dependent on M_{\bullet} for $4 < \beta < 5$, which is typically assumed for the $M_{\bullet} - \sigma$ relation. For simplicity, we ignore the dependence of Γ_{CO} on M_{\bullet} . (2) Γ_{CO} scales linearly with M_{\bullet} , which is more appropriate if the supply rate is set by star formation. In case (1), we calibrate Γ_{CO} to the GC, and we estimate

$$\Gamma_{\text{CO}} = \frac{\gamma_{\text{CO}} N_{\star}(r_{\text{h}})}{t_{\text{NRR}}(r_{\text{h}})} \sim \frac{0.1 \times 10^7}{10^{10} \text{ yr}} = 10^{-4} \text{ yr}^{-1}, \quad (35)$$

where $\gamma_{\text{CO}} = 0.1$ is the fractional number of compact objects formed for a stellar population assuming a top-heavy IMF Löckmann et al. (2010), $N_{\star}(r_{\text{h}}) \sim 10^7$ is the number of stars at the radius of the sphere of influence (Schödel et al. 2014; Feldmeier-Krause et al. 2017; Schödel et al. 2018), and $t_{\text{NRR}}(r_{\text{h}}) \sim 10^{10} \text{ yr}$ is the NRR time-scale at the radius of the sphere of influence (e.g., Merritt 2010). In case (2), we normalize $\Gamma_{\text{CO}} \propto M_{\bullet}$ by the GC top-heavy value that we adopted

in Section 6.2.1, i.e.,

$$\Gamma_{\text{CO}} = \left(\frac{M_{\bullet}}{4 \times 10^6 M_{\odot}} \right) 10^{-4} \text{ yr}^{-1}. \quad (36)$$

Note that, for the GC ($M_{\bullet} = 4 \times 10^6 M_{\odot}$), the two assumptions give the same value of Γ_{CO} .

We assume that the compact object binary formation efficiency f_{CO} is independent of M_{\bullet} , and set it to $f_{\text{CO}} = 0.05$ for a top-heavy IMF, to be consistent with the GC case (Section 6.2.1).

Strictly speaking, the calculated fraction f_{calc} depends on M_{\bullet} since the latter sets the scale of the sphere of influence, thereby the typical outer orbit semimajor axes, and thereby the upper value of a_{in} in the simulations (due to the requirement of dynamical stability). However, this is not a strong effect, with the upper value of a_{in} decreasing to $\sim 10^2 \text{ AU}$ for $M_{\bullet} = 10^4 M_{\odot}$ (see, e.g., Fig. 9), implying that $f_{\text{calc}} = 1/3$. For simplicity, we here set f_{calc} to $1/2$, independent of M_{\bullet} .

With these (strong and uncertain) assumptions, and the data from Table 2 for the merger fractions f_{merge} (adding the fractions for the semisecular and non-semisecular mergers), we plot in Fig. 20 the expected merger rates as a function of M_{\bullet} , for the cases with and without VRR. For $M_{\bullet} \leq 4 \times 10^6 M_{\odot}$, assumption (1) regarding Γ_{CO} gives the highest rates, and in this case we take the data from the simulations for $\gamma = 2$ (giving an upper limit on the merger rates); assumption (2) gives much lower rates, and in this case we take data from the simulations for $\gamma = 1.3$ (giving a lower limit). The areas in between these limits are indicated with shaded regions in Fig. 20.

We emphasize that the rates given in Fig. 20 are highly speculative (note that the error bars reflect the Poisson uncertainty in f_{merge} , but not the much larger uncertainties in the other factors in equation 32, in particular Γ_{CO}). Nevertheless, taken on face value, Fig. 20 indicates that the merger rates are low. For galactic nuclei with low MBH masses (less than a few times $10^4 M_{\odot}$), the rates are higher, in part due the increased enhancement by VRR. However, the existence of such galactic nuclei is not established, and the most optimistic rates still barely reach the lower limit of the rate inferred by LIGO, $12 \text{ Gpc}^{-3} \text{ yr}^{-1}$, and are an order of magnitude lower than the upper LIGO limit, $213 \text{ Gpc}^{-3} \text{ yr}^{-1}$ (Abbott et al. 2017a).

6.3. Comparison to previous work

Here, we compare the results from our Monte Carlo simulations to previous work focussing on the dynamics of binaries in galactic nuclei. The case without VRR has been considered by a number of authors (e.g., Antonini & Perets 2012; Antonini et al. 2014; Prodan et al. 2015; Stephan et al. 2016; Antonini & Rasio 2016; Petrovich & Antonini 2017; Hoang et al. 2018). For our GC-like model, we find a merger fraction of $f_{\text{merge}} = 0.005$ (combining the semisecular and non-semisecular outcomes). This is similar (within a factor of few) to the fraction of Petrovich & Antonini (2017), who find $f_{\text{m}} = 0.0017$ (their table 1, with $\epsilon_z = 0.001$).

On the other hand, Hoang et al. (2018) find much higher merger fractions, of up to $f_{\text{merge}} = 0.15$ for their nominal GC model, which are higher than the merger fractions of Petrovich & Antonini (2017) and our merger fraction by two orders of magnitude. This large difference can be ascribed to different initial conditions. About half of the binaries in Hoang et al. (2018) merge due the gravitational wave emission only (i.e., even in absence of the torque of the MBH). Moreover, Hoang et al. (2018) considered binaries much closer to the

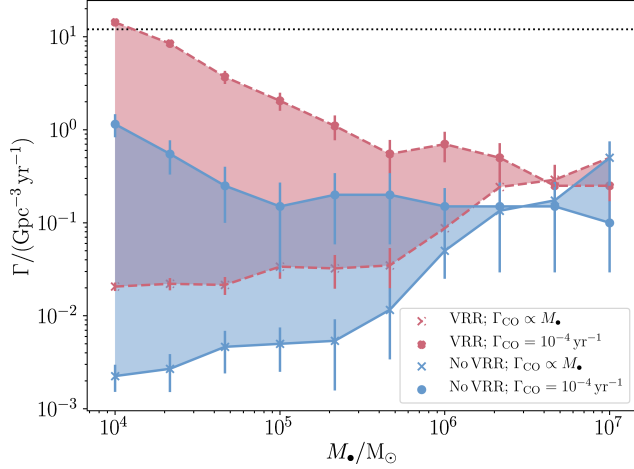


Figure 20. Rough estimates of the merger rates based on equation (32) and the Monte Carlo calculations of Section 5 as a function of $M_•$ for the cases with and without VRR (dashed red lines and solid blue lines, respectively). Here, we either assume that the compact object formation efficiency Γ_{CO} is independent of $M_•$ and equal to 10^{-4} yr^{-1} (bullets), or scales linearly with $M_•$, and normalized such that $\Gamma_{\text{CO}} = [M_• / (4 \times 10^6 M_\odot)] 10^{-4} \text{ yr}^{-1}$ (crosses). The areas in between these cases are shaded with red and blue colors for the simulations with VRR included and not included, respectively. The number density of galaxies is set to a constant $n_{\text{gal}} = 0.02 \text{ Mpc}^{-3}$, and the compact object formation efficiency f_{CO} is assumed to be independent of $M_•$, and set it to $f_{\text{CO}} = 0.045$. The horizontal black dotted line shows the lower LIGO limit of $12 \text{ Gpc}^{-3} \text{ yr}^{-1}$ (Abbott et al. 2017a). The error bars are based on Poisson statistics from the Monte Carlo simulations, i.e., they reflect the uncertainty in f_{merge} , but not the (much larger) errors in the other factors in equation (32), in particular Γ_{CO} .

MBH ($a_{\text{out}}/r_h \sim 10^{-4}$ to $\sim 10^{-2}$) for which the octupole-order terms are important, in contrast to our simulations.

The merger rate predicted by Hoang et al. (2018) is $\sim 1\text{--}3 \text{ Gpc}^{-1} \text{ yr}^{-1}$, which is one (two) orders of magnitude larger than our GC rate estimate without VRR assuming a top heavy (canonical) IMF. This can be ascribed to the following.

1. The merger fraction adopted by Hoang et al. (2018) is $f_{\text{merge}} = 0.15$, which is $0.15/0.005 = 30$ times larger than our adopted fraction.
2. The ‘conversion’ factor from merger fraction to rate adopted by Hoang et al. (2018) is $\Gamma/f_{\text{merge}} = 2/0.15 \text{ Gpc}^{-1} \text{ yr}^{-1} \approx 13 \text{ Gpc}^{-1} \text{ yr}^{-1}$. We assumed a ‘conversion’ factor of $\Gamma/f_{\text{merge}} = 2.5 \text{ Gpc}^{-1} \text{ yr}^{-1}$ and $\Gamma/f_{\text{merge}} = 50 \text{ Gpc}^{-1} \text{ yr}^{-1}$ for the canonical and top-heavy IMF, respectively.

These two points combined explain the different merger rates.

In calculating their rates, Hoang et al. (2018) assumed that there exists a steady-state population of BH-BH binaries in the central 0.1 pc, with a number of $N_{\text{steady}} = 200$ corresponding to a merger rate of $2 \text{ Gpc}^{-1} \text{ yr}^{-1}$. This requires replenishment of the BH-BH binaries on a time-scale of 100 Myr, which would be consistent with in-situ star-formation in a disk of massive O/B stars close to the MBH (e.g., Bartko et al. 2009). In our rate calculation, we assumed a global influx of compact objects, which is more appropriate in our situation given that

we considered a binary population at larger distances from the MBH.

VanLandingham et al. (2016) were the first to consider the combined effects of VRR and LK evolution by means of hybrid N -body methods. Due to computational limitations, the MBH masses were limited to up to $10^4 M_\odot$. VanLandingham et al. (2016) found high merger fractions in their simulations. This is consistent with our results, in the sense that we find that the enhancement due to VRR is most significant for low MBH masses. More quantitatively, VanLandingham et al. (2016) found a merger fraction of ≈ 0.25 in their simulation with $M_• = 10^4 M_\odot$ (10k stars). This is very similar to our merger fraction of ≈ 0.29 for the case $M_• = 10^4 M_\odot$ and $\gamma = 2$ (adding the semisecular and non-semisecular fractions). This apparent agreement may be fortuitous, however, given that we did not consider a number of potentially important effects (see Section 6.1). In particular, DF is an important process in the simulations of VanLandingham et al. (2016); prior to their merger, most merging binaries sink inwards to the MBH. DF could therefore be important for bringing a binary from a regime with $\mathcal{R} \gg 1$, where LK-VRR coupling is unimportant, to a region in which $\mathcal{R} \sim 1$, where LK-VRR evolution can drive the binary to merge.

We remark that VanLandingham et al. (2016) extrapolated their results to higher MBH masses similar to the MBH in the GC, and found high merger rates of $\sim 100 \text{ Gpc}^{-3} \text{ yr}^{-1}$. Our results show that the merger fraction decreases rapidly with increasing MBH mass. Therefore, one should be cautious when extrapolating rates from lower to higher MBH masses. In particular, the rate of $100 \text{ Gpc}^{-3} \text{ yr}^{-1}$ found by VanLandingham et al. (2016) may have been overestimated.

7. CONCLUSIONS

We considered the effect of torques induced by stars around an MBH (specifically, VRR), on the LK dynamics of binaries near MBHs. We showed that VRR can increase the rates of strong interactions in binaries orbiting the MBH by inducing high mutual inclinations between the inner orbit of the binary and the outer orbit of the binary around the MBH. Consequently, the binary can be driven to high eccentricities through the LK mechanism, even if the initial mutual inclination between the inner and outer orbits is small. These strong interactions include orbital energy loss due to GW emission, implying that VRR can enhance the rates of compact mergers in galactic nuclei, with implications for the detection of GWs. Our main conclusions are listed below.

1. VRR can enhance the efficiency of the LK mechanism if the VRR and LK time-scales are comparable. We explored the associated parameter space in Section 2, and found that the ‘regions of interest’, i.e., the parameter space in which the VRR and LK time-scales are similar, is largest for small MBH masses ($\sim 10^4 M_\odot$), steep stellar density profiles ($\gamma \approx 2$; $\rho_\star \propto r^{-\gamma}$), and wide inner binary orbits ($a_{\text{in}} \gtrsim 10 \text{ AU}$). This can be understood qualitatively by noting that the VRR time-scale increases relatively to the LK time-scale with increasing MBH mass. Furthermore, for tight inner binary orbits ($a_{\text{in}} \lesssim 1 \text{ AU}$), PN precession in the inner binary orbit quenches LK oscillations, regardless of VRR. Also, the regions of interest are typically far away from the MBH (close to the radius of the sphere of influence), where octupole-order terms are unimportant.
2. Using a simplified model for VRR, we numerically integrated the secular equations of motion for the three-body

binary-MBH dynamics coupled with the effects of VRR on the barycenter of the outer binary (Section 4). We determined the eccentricity distributions as a function of the ‘adiabatic parameter’ $\mathcal{R} \equiv t_{\text{LK}}/t_{\text{VRR}}$. If $\mathcal{R} \ll 1$, then the binary-MBH system is effectively decoupled from the torques induced by the stellar background, and the canonical LK dynamics apply (in particular, only high eccentricities can be induced if the initial mutual inclination is close to 90°). If $\mathcal{R} \sim 1$, then the dynamics are typically chaotic, and very high eccentricities can be attained on time-scales of $\sim 10 - 100 t_{\text{LK}}$. If $\mathcal{R} \gg 1$, then LK oscillations are suppressed, although there is diffusive evolution of the eccentricity on long time-scales, on the order of $\mathcal{R} t_{\text{LK}}$.

3. We carried out Monte Carlo calculations of BH-BH binaries in galactic nuclei in Section 5, taking into account the coupled LK and VRR evolution, PN corrections, and binary evaporation. Consistent with the time-scale arguments of Section 2, we found that VRR is effective at enhancing the rates of BH mergers for low MBH masses and steep density profiles. For $M_\bullet = 10^4 M_\odot$ and a density slope of $\gamma = 2$, the merger enhancement in terms of the delay-time distribution (Fig. 19) is typically a factor of ~ 10 , up to ~ 60 compared to the case of canonical LK dynamics. In both cases, the merger rates decrease with time approximately as t^{-1} . The merger fractions in our simulations with VRR included range from less than a per cent for high MBH masses ($M_\bullet \gtrsim 10^6 M_\odot$), to up to $\simeq 30\%$ (for $M_\bullet = 10^4 M_\odot$ and $\gamma = 2$). These fractions are a factor of a few to ~ 10 times larger compared to the situation in which VRR is not taken into account.

4. Although the merger of the inner BH-BH binary is triggered by high eccentricity, when reaching the LIGO band the inner orbit eccentricity is highly damped due to GW emission. Some signature remains in the distribution of $e_{\text{in,LIGO}}$, although it is small compared to other dynamical formation channels: the median $e_{\text{in,LIGO}}$ in the simulations with VRR included is $\sim 10^{-5}$, compared to $\sim 10^{-6}$ in the canonical LK case (see Fig. 13). The highest $e_{\text{in,LIGO}}$ are attained in systems that also entered the semisecular regime, in which the double orbit averaging approximation formally breaks down.

5. Large uncertainties are involved in the process of converting merger fractions found in the Monte Carlo simulations to absolute BH-BH merger rates. Nevertheless, we estimated the merger rates for the GC and for galactic nuclei with different MBH masses, by making two limiting assumptions on the formation rate of compact objects. With our assumptions, we find that the GC merger rates are about two orders of magnitude lower than the lower limit inferred by LIGO, $12 \text{ Gpc}^{-3} \text{ yr}^{-1}$ (Abbott et al. 2017a), if only LK dynamics are included. With the inclusion of VRR, the rate enhancement is only small, i.e., a factor of ~ 1.6 , suggesting that LK-VRR coupling cannot explain merger rates for galactic nuclei with masses comparable to the MBH in the GC. The absolute rates and the enhancement by VRR generally increase with decreasing MBH mass. Nonetheless, even in our most optimistic scenario, the baseline BH-BH merger rate for other MBH masses is small, and the enhancement by LK-VRR coupling is not large enough to increase the rate to well above the LIGO/VIRGO lower limit. For $M_\bullet = 10^4 M_\odot$, the rate barely reaches $12 \text{ Gpc}^{-3} \text{ yr}^{-1}$, and is an order of magnitude lower than the upper LIGO limit, $213 \text{ Gpc}^{-3} \text{ yr}^{-1}$ (Abbott et al. 2017a).

ACKNOWLEDGEMENTS

We thank Hagai Perets, Bence Kocsis, Lisa Randall, Scott Tremaine, and Bao-Minh Hoang for stimulating discussions and comments on our manuscript. We also thank the anonymous referee for a helpful and detailed report. In memoriam Yoshihide Kozai (April 1 1928 — February 5 2018). ASH gratefully acknowledges support from the Institute for Advanced Study, the Peter Svennilson Membership, and from NASA grant NNX14AM24G. BB acknowledges support from the Schmidt Fellowship. CP acknowledges support from the Gruber Foundation Fellowship and Jeffrey L. Bishop Fellowship. FA acknowledges support from an E. Rutherford fellowship (ST/P00492X/1) from the Science and Technology Facilities Council.

REFERENCES

- Abbott, B. P., Abbott, R., Abbott, T. D., et al. 2016a, *Physical Review Letters*, 116, 241103
— 2016b, *Physical Review Letters*, 116, 061102
— 2017a, *Physical Review Letters*, 118, 221101
— 2017b, *ApJL*, 851, L35
— 2017c, *Physical Review Letters*, 119, 141101
— 2017d, *ApJL*, 848, L12
Aharon, D., Mastrobuono Battisti, A., & Perets, H. B. 2016, *ApJ*, 823, 137
Aharon, D., & Perets, H. B. 2015, *ApJ*, 799, 185
Alexander, T., & Bar-Or, B. 2017, *Nature Astronomy*, 1, 0147
Alexander, T., & Hopman, C. 2009, *ApJ*, 697, 1861
Alexander, T., & Pfuhl, O. 2014, *ApJ*, 780, 148
Aller, M. C., & Richstone, D. 2002, *AJ*, 124, 3035
Antognini, J. M. O. 2015, *MNRAS*, 452, 3610
Antonini, F., & Merritt, D. 2013, *ApJL*, 763, L10
Antonini, F., Murray, N., & Mikkola, S. 2014, *ApJ*, 781, 45
Antonini, F., & Perets, H. B. 2012, *ApJ*, 757, 27
Antonini, F., & Rasio, F. A. 2016, *ApJ*, 831, 187
Antonini, F., Rodriguez, C. L., Petrovich, C., & Fischer, C. L. 2017a, *ArXiv e-prints*, arXiv:1711.07142
Antonini, F., Toonen, S., & Hamers, A. S. 2017b, *ApJ*, 841, 77
Arca-Sedda, M., & Capuzzo-Dolcetta, R. 2017, *ArXiv e-prints*, arXiv:1709.05567
Arca-Sedda, M., & Gualandris, A. 2018, *MNRAS*, 477, 4423
Askar, A., Szkudlarek, M., Gondek-Rosińska, D., Giersz, M., & Bulik, T. 2017, *MNRAS*, 464, L36
Bar-Or, B., & Alexander, T. 2014, *Classical and Quantum Gravity*, 31, 244003
— 2016, *ApJ*, 820, 129
Bar-Or, B., & Fouvry, J.-B. 2018, *ArXiv e-prints*, arXiv:1802.08890
Bartko, H., Martins, F., Fritz, T. K., et al. 2009, *ApJ*, 697, 1741
Belczynski, K., Buonanno, A., Cantiello, M., et al. 2014, *ApJ*, 789, 120
Belczynski, K., Holz, D. E., Bulik, T., & O’Shaughnessy, R. 2016, *Nature*, 534, 512
Belczynski, K., Klencki, J., Meynet, G., et al. 2017, *ArXiv e-prints*, arXiv:1706.07053
Binney, J., & Tremaine, S. 2008, *Galactic Dynamics: Second Edition* (Princeton University Press)
Brown, D. A., & Zimmerman, P. J. 2010, *Phys. Rev. D*, 81, 024007
Conselice, C. J., Blackburne, J. A., & Papovich, C. 2005, *ApJ*, 620, 564
de Mink, S. E., & Mandel, I. 2016, *MNRAS*, 460, 3545
Dominik, M., Belczynski, K., Fryer, C., et al. 2012, *ApJ*, 759, 52
— 2013, *ApJ*, 779, 72
Duchêne, G., & Kraus, A. 2013, *ARA&A*, 51, 269
East, W. E., McWilliams, S. T., Levin, J., & Pretorius, F. 2013, *Phys. Rev. D*, 87, 043004
Eilon, E., Kupi, G., & Alexander, T. 2009, *ApJ*, 698, 641
Faber, S. M., & Jackson, R. E. 1976, *ApJ*, 204, 668
Feldmeier-Krause, A., Zhu, L., Neumayer, N., et al. 2017, *MNRAS*, 466, 4040
Fouvry, J.-B., Pichon, C., & Magorrian, J. 2017, *A&A*, 598, A71
Fragione, G., & Kocsis, B. 2018, *ArXiv e-prints*, arXiv:1806.02351
Fritz, T. K., Chatzopoulos, S., Gerhard, O., et al. 2016, *ApJ*, 821, 44
Ghez, A. M., Salim, S., Weinberg, N. N., et al. 2008, *ApJ*, 689, 1044
Gillessen, S., Eisenhauer, F., Trippe, S., et al. 2009, *ApJ*, 692, 1075
Gondán, L., Kocsis, B., Raffai, P., & Frei, Z. 2018, *ApJ*, 860, 5

- Grishin, E., Lai, D., & Perets, H. B. 2018, *MNRAS*, 474, 3547
- Hamers, A. S., & Lai, D. 2017, *MNRAS*, 470, 1657
- Hamers, A. S., & Portegies Zwart, S. F. 2016, *MNRAS*, 459, 2827
- Hamers, A. S., Portegies Zwart, S. F., & Merritt, D. 2014, *MNRAS*, 443, 355
- Heggie, D. C. 1975, *MNRAS*, 173, 729
- Heggie, D. C., Hut, P., & McMillan, S. L. W. 1996, *ApJ*, 467, 359
- Hills, J. G. 1988, *Nature*, 331, 687
- Hoang, B.-M., Naoz, S., Kocsis, B., Rasio, F. A., & Dosopoulou, F. 2018, *ApJ*, 856, 140
- Hopman, C., & Alexander, T. 2006, *ApJ*, 645, 1152
- Huerta, E. A., & Brown, D. A. 2013, *Phys. Rev. D*, 87, 127501
- Hurley, J. R., Tout, C. A., & Pols, O. R. 2002, *MNRAS*, 329, 897
- Hut, P. 1993, *ApJ*, 403, 256
- Innanen, K. A., Zheng, J. Q., Mikkola, S., & Valtonen, M. J. 1997, *AJ*, 113, 1915
- Jeans, J. H. 1919, *MNRAS*, 79, 408
- Kalogera, V., Belczynski, K., Kim, C., O’Shaughnessy, R., & Willems, B. 2007, *Phys. Rep.*, 442, 75
- Katz, B., Dong, S., & Malhotra, R. 2011, *Physical Review Letters*, 107, 181101
- Kimpson, T. O., Spera, M., Mapelli, M., & Ziosi, B. M. 2016, *MNRAS*, 463, 2443
- Kinoshita, H., & Nakai, H. 1999, *Celestial Mechanics and Dynamical Astronomy*, 75, 125
- Kobulnicky, H. A., Kiminki, D. C., Lundquist, M. J., et al. 2014, *ApJS*, 213, 34
- Kocsis, B., & Tremaine, S. 2011, *MNRAS*, 412, 187
- . 2015, *MNRAS*, 448, 3265
- Kopparapu, R. K., Hanna, C., Kalogera, V., et al. 2008, *ApJ*, 675, 1459
- Kozai, Y. 1962, *AJ*, 67, 591
- Li, G., Naoz, S., Holman, M., & Loeb, A. 2014, *ApJ*, 791, 86
- Lidov, M. L. 1962, *Planet. Space Sci.*, 9, 719
- Lithwick, Y., & Naoz, S. 2011, *ApJ*, 742, 94
- Liu, B., & Lai, D. 2017, *ApJL*, 846, L11
- . 2018, *ArXiv e-prints*, arXiv:1805.03202
- Löckmann, U., Baumgardt, H., & Kroupa, P. 2010, *MNRAS*, 402, 519
- Lower, M. E., Thrane, E., Lasky, P. D., & Smith, R. 2018, *ArXiv e-prints*, arXiv:1806.05350
- Mandel, I., & de Mink, S. E. 2016, *MNRAS*, 458, 2634
- Mapelli, M. 2016, *MNRAS*, 459, 3432
- Marchant, P., Langer, N., Podsiadlowski, P., Tauris, T. M., & Moriya, T. J. 2016, *A&A*, 588, A50
- Mardling, R. A., & Aarseth, S. J. 2001, *MNRAS*, 321, 398
- Merritt, D. 2010, *ApJ*, 718, 739
- . 2013, *Dynamics and Evolution of Galactic Nuclei* (Princeton University Press)
- Merritt, D., Alexander, T., Mikkola, S., & Will, C. M. 2011, *Phys. Rev. D*, 84, 044024
- Merritt, D., & Ferrarese, L. 2001, *ApJ*, 547, 140
- Naoz, S. 2016, *ARA&A*, 54, 441
- Naoz, S., Kocsis, B., Loeb, A., & Yunes, N. 2013, *ApJ*, 773, 187
- O’Leary, R. M., Rasio, F. A., Fregeau, J. M., Ivanova, N., & O’Shaughnessy, R. 2006, *ApJ*, 637, 937
- Öpik, E. 1924, *Publications of the Tartu Astrofizica Observatory*, 25
- Park, D., Kim, C., Lee, H. M., Bae, Y.-B., & Belczynski, K. 2017, *MNRAS*, 469, 4665
- Perets, H. B. 2009, *ApJ*, 690, 795
- Perets, H. B., Gualandris, A., Kupa, G., Merritt, D., & Alexander, T. 2009, *ApJ*, 702, 884
- Peters, P. C. 1964, *Physical Review*, 136, 1224
- Petrovich, C., & Antonini, F. 2017, *ApJ*, 846, 146
- Portegies Zwart, S. F., & McMillan, S. L. W. 2000, *ApJL*, 528, L17
- Prodan, S., Antonini, F., & Perets, H. B. 2015, *ApJ*, 799, 118
- Randall, L., & Xianyu, Z.-Z. 2018a, *ArXiv e-prints*, arXiv:1802.05718
- . 2018b, *ApJ*, 853, 93
- Rauch, K. P., & Tremaine, S. 1996, *New A*, 1, 149
- Rodríguez, C. L., Amaro-Seoane, P., Chatterjee, S., & Rasio, F. A. 2018, *Physical Review Letters*, 120, 151101
- Rodríguez, C. L., Chatterjee, S., & Rasio, F. A. 2016, *Phys. Rev. D*, 93, 084029
- Rodríguez, C. L., Morscher, M., Pattabiraman, B., et al. 2015, *Physical Review Letters*, 115, 051101
- Salpeter, E. E. 1955, *ApJ*, 121, 161
- Samsing, J. 2018, *Phys. Rev. D*, 97, 103014
- Samsing, J., Askar, A., & Giersz, M. 2017a, *ArXiv e-prints*, arXiv:1712.06186
- Samsing, J., MacLeod, M., & Ramirez-Ruiz, E. 2017b, *ArXiv e-prints*, arXiv:1706.03776
- Samsing, J., & Ramirez-Ruiz, E. 2017, *ApJL*, 840, L14
- Sana, H., de Mink, S. E., de Koter, A., et al. 2012, *Science*, 337, 444
- Schnittman, J. D. 2004, *Phys. Rev. D*, 70, 124020
- Schödel, R., Feldmeier, A., Kunneriath, D., et al. 2014, *A&A*, 566, A47
- Schödel, R., Gallego-Cano, E., Dong, H., et al. 2018, *A&A*, 609, A27
- Sigurdsson, S., & Hernquist, L. 1993, *Nature*, 364, 423
- Silber, K., & Tremaine, S. 2017, *ApJ*, 836, 39
- Spitzer, L. 1987, *Dynamical evolution of globular clusters*
- Sridhar, S., & Touma, J. R. 2016a, *MNRAS*, 458, 4129
- . 2016b, *MNRAS*, 458, 4143
- Stephan, A. P., Naoz, S., Ghez, A. M., et al. 2016, *MNRAS*, 460, 3494
- Teyssandier, J., Naoz, S., Lizarraga, I., & Rasio, F. A. 2013, *ApJ*, 779, 166
- Tutukov, A., & Yungelson, L. 1973, *Nauchnye Informatsii*, 27, 70
- Tutukov, A. V., & Yungelson, L. R. 1993, *MNRAS*, 260, 675
- Ulubay-Siddiki, A., Gerhard, O., & Arnaboldi, M. 2009, *MNRAS*, 398, 535
- VanLandingham, J. H., Miller, M. C., Hamilton, D. P., & Richardson, D. C. 2016, *ApJ*, 828, 77
- Voss, R., & Tauris, T. M. 2003, *MNRAS*, 342, 1169
- Weinberg, S. 1972, *Gravitation and Cosmology: Principles and Applications of the General Theory of Relativity* (Wiley India Pvt. Limited), 688
- Wen, L. 2003, *ApJ*, 598, 419
- Ziosi, B. M., Mapelli, M., Branchesi, M., & Tormen, G. 2014, *MNRAS*, 441, 3703